Robotic-Assistive Needle Platform with Bio-impedance and Multi-Modal Sensing for Biomedical Applications

Qingyu Zhang

A transfer thesis submitted in partial fulfilment

of the requirements for the degree of

Doctor of Philosophy

of

University College London

Sensor Systems and Circuits Research Group

Department of Electronic and Electrical Engineering

University College London

Principal Supervisor: Dr. Yu Wu

Subsidiary Supervisor: Prof. Andreas Demosthenous

word counts: 13774

Date: 01/06/2025

ACKNOWLEDGEMENT

I would like to express my deepest gratitude to my principal supervisor, Dr. Yu Wu, and my co-supervisor, Prof. Andreas Demosthenous, for their unwavering support and expert guidance throughout my research journey. Their insights have been invaluable in shaping both my technical skills and my academic mindset.

I am also especially grateful to Dr. Ahmed A-Hindawi for his thoughtful suggestions and for taking the time to introduce me to hands-on central venous catheter (CVC) training and ultrasound imaging from fundamental medical perspectives. His mentorship helped me gain a deeper understanding of how our system integrates with existing clinical practices.

I would also like to thank every member of our research group. Whenever I faced challenges, their patience, advice, and practical assistance were invaluable. Their camaraderie and willingness to share knowledge created an environment in which I always felt supported.

I look forward to continuing my work under their mentorship and to learning even more from their expertise as I embark on my PhD studies.

ABSTRACT

Using standard needle guidance with ultrasound (US), computed tomography (CT), or magnetic resonance imaging (MRI) has drawbacks and may cause issues like puncturing a blood vessel, causing pneumothorax, or damaging a nerve. This phenomenon is more common for an inexperienced participant. Therefore, a guidance technology that boosts needle insertion accuracy while integrating seamlessly into existing clinical workflows is essential.

The integration of advanced sensory modalities into medical instruments offers a promising solution. For needle sensing specifically, compared to biomechanical, optical, and magnetic approaches, bioimpedance (BIOZ) offers not only real-time tissue classification but also miniaturisation capabilities. However, existing BIOZ-based needle systems face two key challenges: suboptimal electrode designs that lead to measurement drift and a limited effective sensitivity zone, where impedance information is confined to the immediate vicinity of the electrode surface.

This research aims to develop a system that combines advanced BIOZ sensing methods, robotic touch feedback, and ultrasound signal processing to accurately guide needles during deep insertion procedures. Unlike current user-interpreted ultrasound imaging methods, the proposed system will actively characterise tissue properties and provide real-time guidance for needle positioning, targeting sub-millimetre insertion accuracy through intelligent sensor fusion.

Initial prototype validation demonstrates the approach's feasibility for the CVC procedures. Along the z-axis, the prototype system achieved a 100% venous entry success rate and 86.7% central positioning accuracy. Across 24 trials, the system maintained sub-millimetre precision with an RMS error of 0.66 mm while providing real-time feedback at over 100 Hz sampling rate.

This work establishes the technological foundation for next-generation minimally invasive procedures. The platform's compatibility with existing clinical workflows and standard instruments

supports practical adoption, with potential applications extending to targeted drug delivery, biopsy guidance, and neuro-interventions. By enabling precise tissue characterisation without relying solely on external imaging, this research advances precision medicine while reducing procedural complexity and improving patient safety outcomes.

Keywords: Bioimpedance needle, central venous catheterisation, haptic-assistive device, human-machine interface, robotic-assisted surgery, venous entry detection

ABBREVIATIONS

ADC : Analogue-to-Digital Converter

AFE : Analogue Front-End

AME : Advanced Measurement Equipment

AR : Augmented Reality

BIOZ : Bioimpedance

BiNH : BIOZ Needle Handle

BLE : Bluetooth Low Energy

CE : Counter Electrode

CF : Crest Factor

CMFB : Common-Mode Feedback

CMOS : Complementary Metal Oxide Semiconductor

CT : Computed Tomography

CVC : Central Venous Catheter

DAC : Digital-to-Analog Converter

DFT : Discrete Fourier Transform

DLC : Double-Layer Capacitance

DOF : Degrees of Freedom

DOI : Depth of Investigation

DVA : Difficult Venous Access

EIT : Electrical Impedance Tomography

EM : Electromagnetic

FEM : Finite Element Method

FBG : Fibre Bragg Grating

FPC : Flexible Printed Circuit

FS : Force Sensing

GUI : Graphical User Interface

HMI : Human-Machine Interface

IA : Instrumentation Amplifier

IDE : Interdigitated Electrodes

IHP : Inner Helmholtz Plane

IMU : Inertial Measurement Unit

LCR : Inductance, Capacitance, Resistance

MRI : Magnetic Resonance Imaging

NIR : Near-Infrared

OCT : Optical Coherence Tomography

OHP : Outer Helmholtz Plane

OTA : Operational Transconductance Amplifier

PCB : Printed Circuit Board

PEG : Polyethylene Glycol

PIVC : Peripheral Intravenous Catheter

PZT : Lead Zirconium Titanate

RE : Reference Electrode

RVC : Retinal Vein Cannulation

SNR : Signal-to-Noise Ratio

SPL : Selective Passivation Layer

TIA : Transimpedance Amplifier

US : Ultrasound

VOC : Voltage-Controlled Oscillator

VR : Virtual Reality

WE : Working Electrode

Table of Contents

1. INTRODUCTION

This chapter presents the background of my PhD research, explaining the motivation behind the study and the specific research problem it aims to address. It further defines the research aims, details the specific objectives, and outlines the expected contributions and societal impact. Additionally, it provides a concise overview of the structure of this report.

1.1 Research Background

The integration of novel sensors with medical instruments represents a pivotal trend in modern healthcare, driving rapid advancements in capabilities for physiological monitoring, surgical assistance, disease diagnosis, and patient surveillance [1]. Continuous innovations have yielded a growing array of sensor-enhanced devices, including precision needles, flexible endoscopes, robotic surgical tools, and swallowable diagnostic capsules. Each of these platforms leverages sensing technologies to extend clinician perception beyond the limits of unaided vision and touch.

Medical needles remain among the most ubiquitous clinical tools, with over 16 billion injections administered worldwide each year [2]. Despite established guidelines on needle gauge selection for various procedures, there are no universally accepted standards governing insertion accuracy or path planning. Clinicians must therefore rely on subjective visualisation of tissue deformation and imprecise tactile feedback to guide needle advancement [3]. Improper needle placement can lead to procedural complications and patient discomfort, particularly in high-precision interventions. Specifically, 2012 statistics report that central venous catheterisation (CVC) performed without ultrasound (US) guidance had complication rates approaching 19.5%, including inadvertent venous puncture, arterial mispuncture, local haematoma, nerve injury, pneumothorax, catheter misplacement, and deep vein thrombosis [4]–[6]. Advances in medical practice and the adoption of

the US have reduced the overall CVC complication rate to 3.02% [6]. However, the US guidance demands experienced operators to ensure proper hand–eye coordination, and Lennon et al. found that practitioners with more than 25 prior procedures achieved significantly fewer complications [4], [7]. Percutaneous lung biopsy (PLB) illustrates similar challenges. Overall complication rates, including any mild or severe event, average 10.6% [8]. While for subsolid lung nodules, the rate could reach 43%, including a severe complications rate of 0.1% [9]. While mild complications are common, careful needle path planning can greatly improve patient recovery and comfort. Computed tomography (CT) guidance is used for biopsy, but its limited real-time capabilities often prolong patient discomfort during insertion [10]. Moreover, the spatial resolution of CT and US can make it challenging to delineate precise tissue boundaries. By contrast, magnetic resonance imaging (MRI) offers superior soft-tissue contrast and avoids ionising radiation, but its application in needle-based procedures is constrained by the need for MRI-compatible needles and the lack of real-time, high-resolution imaging [11]. Li et al. reported one mild complication in their series of 16 US fusion-guided core needle biopsies of head and neck lesions. This low complication rate nonetheless illustrates the importance of highly precise needle guidance in these high-risk regions, where there is no margin for failure [12]. Consequently, there is a pressing need for devices that provide high-resolution, real-time, and precise navigation, thereby enhancing safety in resource-limited settings, reducing training costs, and delivering more reliable procedural outcomes.

To address those limitations, researchers develop different sensor systems based on the fact that different tissues exhibit distinct mechanical properties, protein compositions, optical refractive indices and electrical conductivities [1], [13]. These include biomechanical, optical, magnetic and bioelectrical methods. Accurate needle localisation and visualisation are crucial for precise positioning during medical procedures. While direct needle insertion with a tissue-type classification sensor is common, precise trajectory guidance is essential for deep tissue penetration [3]. As the length of the needle increases, tissue resistance and friction may cause needle bending, which can

lead to incorrect needle placement [1]. Furthermore, accurate path planning helps avoid harming sensitive structures, such as nerves, lymph, and other delicate regions, thereby minimising patient discomfort and reducing the risk of complications [14].

Despite substantial advances in individual sensing technologies and proof-of-concept demonstrations, the development of fully integrated, clinically validated smart needle systems suitable for routine deployment remains a significant challenge. Future research endeavours should prioritise the seamless integration of multimodal sensors to establish broad compatibility with existing clinical workflows and instrumentation. At the same time, provide accurate and real-time feedback for safer insertion. In addition, successfully addressing both technical and regulatory challenges will be instrumental in facilitating the translation of smart-needle innovations from laboratory research environments to routine clinical implementation, ultimately enhancing procedural accuracy, improving patient safety outcomes, and advancing the standard of minimally invasive medical care.

1.2 Research Aim

The overarching objective of this research is to develop an integrated multi-modal sensing platform for needle insertion procedures. Mainly for needle insertion applications, especially for those who need deep insertion. The proposed system aims to maintain superior insertion precision through the synergistic integration of bioimpedance (BIOZ), ultrasound imaging and a haptic robotic assistance system. The target is to achieve sub-millimetre insertion accuracy in three-dimensional spatial trajectory control and provide haptic feedback via a robotic system during deep tissue needle placement.

1.3 Research Objectives

To fulfil the research aim outlined above, the following specific objectives are proposed:

- **Achieve reliable tissue classification using bioimpedance sensing at the needle tip.** Develop and validate bioimpedance-based tissue differentiation capabilities that can distinguish between different tissues during needle insertion. Improving the sensing area on the tiny needle surface. This includes the needle sensor probe design with optimised electrode layouts, measurement strategy and conductivity matrix reconstruction algorithm. It also comes with ultra-low-noise, high-sensitivity readout circuits with wireless communication capabilities that meet the stringent performance and portability requirements of clinical needle-based procedures.

- **Develop sensor fusion algorithms for enhanced needle guidance.** Create intelligent integration of bioimpedance and ultrasound image data to provide comprehensive real-time guidance during CVC procedures, improving upon single-modality approaches.

- **Integrate haptic feedback to enhance insertion precision and safety.** Implement haptic-enabled guidance systems that provide real-time force feedback to clinicians, enabling sub-millimetre accuracy in three-dimensional needle trajectory control.

1.4 Research Contribution and Value

This research would make three contributions. First is trying to cut the edge of the outer electrical impedance tomography (OEIT) system. The small sensitivity area is the critical limitation for this system. We would introduce different electrode layouts and optimise the injection strategy. A more complex sensitivity matrix with detailed conductivity info could also be obtained. By proposing a new demodulation algorithm and a finite element analysis algorithm, we can achieve the detection of conductivity distribution in a larger space.

Meanwhile, we fuse impedance readings with ultrasound images. We apply reinforcement learning to these continuous data streams and incorporate diffusion-model predictions. Together, they enable the construction of a neural-scale 3D model. This approach overcomes the limitation of current models,

which focus solely on macroscopic physiological structures.

Additionally, we will couple a simplified viscoelastic tissue model with a needle-tip interaction law to drive a real-time haptic interface. The system continuously computes an optimal 3D trajectory—based on local stiffness gradients and proximity to critical structures—and renders force feedback that gently redirects the needle whenever it approaches sensitive anatomy. By blending fast, precomputed tissue responses with on-the-fly path adjustment, this approach delivers smooth, clinically realistic tactile cues and helps operators maintain safe insertion angles throughout the procedure.

Clinically, this continuous-monitoring, haptic-feedback system enables early detection and real-time correction of insertion errors. Combined, these features deliver sub-millimetre trajectory precision and greatly minimise the risk of puncturing organs, vessels, nerves or other vital tissues. By providing intuitive guidance even during deep or complex needle paths, the system markedly lowers overall complication rates.

1.5 Report Organisation

This transfer report is structured into four chapters. The current chapter introduces the background of the research, followed by the research aim, objectives, motivation, and potential impact.

Chapter 2 reviews different sensor configurations used in needle-based systems. These configurations incorporate various sensing techniques, including biomechanical, optical, magnetic and BIOZ modalities. This chapter also explains the rationale for selecting the BIOZ approach for this research and provides essential background knowledge on BIOZ.

Chapter 3 presents a prototype of the proposed device, demonstrating the feasibility of the core concept and validating the system's foundational design.

Finally, Chapter 4 outlines the ongoing and future work, including recent results, a detailed timeline for the remainder of the PhD, and planned efforts to increase the research's impact—such as extended experiments, academic publications, and workshops.

2. LITERATURE REVIEW

2.1 Comparison of Different Strategies

The limitations of conventional clinical imaging techniques have been outlined in the background section. This chapter further explores advanced sensing approaches that have been proposed to overcome these limitations. Specifically, it reviews four major categories of sensing modalities: biomechanical, optical, magnetic, and bioimpedance (BIOZ), including electrochemical sensors. These systems differ in both sensor placement and functional capabilities, and their classification is summarised in Fig. 2.1.

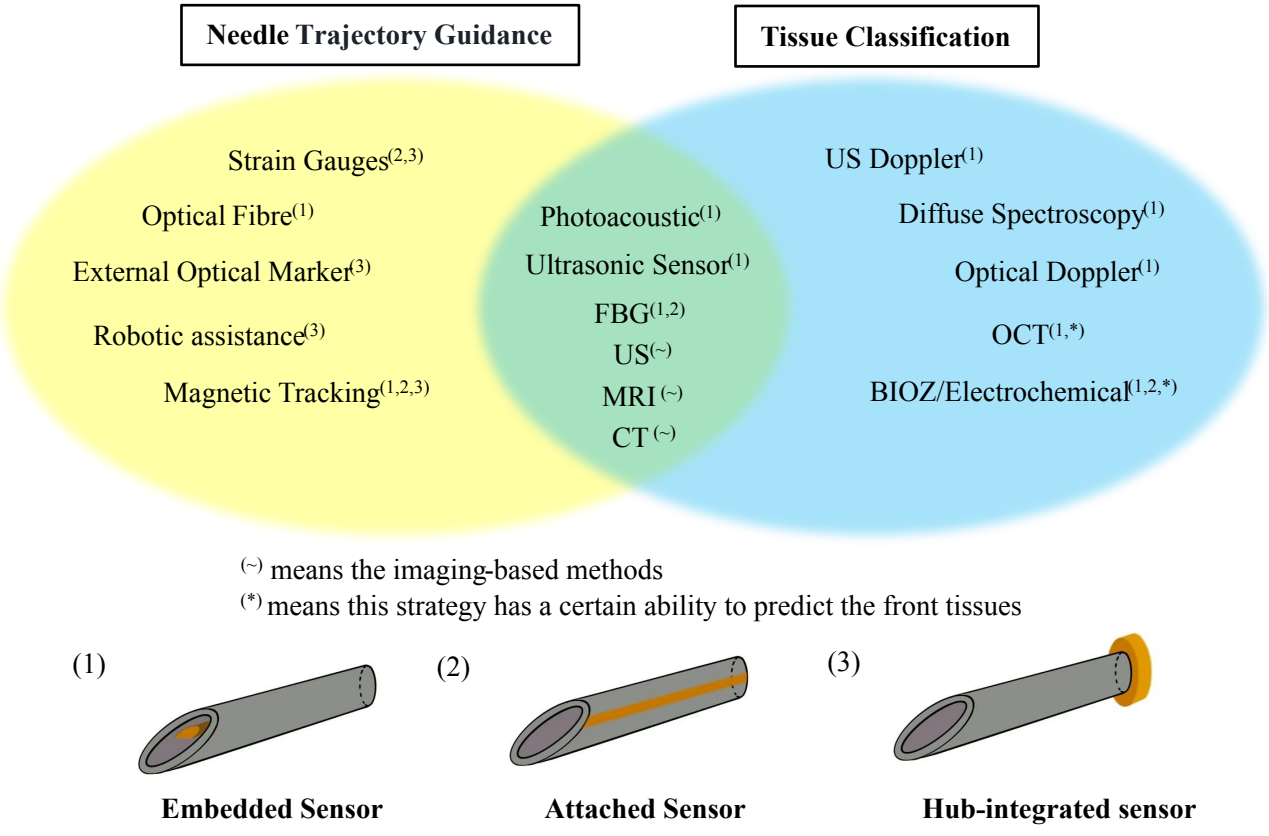

Fig. 2.1. Sensing technologies for needle-based interventions are broadly categorised into two main functional domains: needle trajectory guidance and tissue classification. Depending on their purpose, these systems enable spatial tracking, tissue differentiation, or both. Their physical integration with the needle is illustrated through various implementation strategies, including embedded sensors, surface-attached sensors, hub-integrated sensors, and externally guided imaging-based methods.

2.1.1 Biomechanical

Different tissues exhibit distinct mechanical properties, including stiffness, elasticity, viscosity, and acoustic impedance. For instance, tissues such as bone and tendon are classified as hard tissues, whereas blood vessels and adipose tissue are considered soft tissues. One of the most widely adopted applications based on these mechanical differences is ultrasound elastography, which is commonly used in cancer diagnostics—particularly for prostate cancer—due to the fact that malignant regions often exhibit significantly higher stiffness compared to surrounding healthy tissue [15].

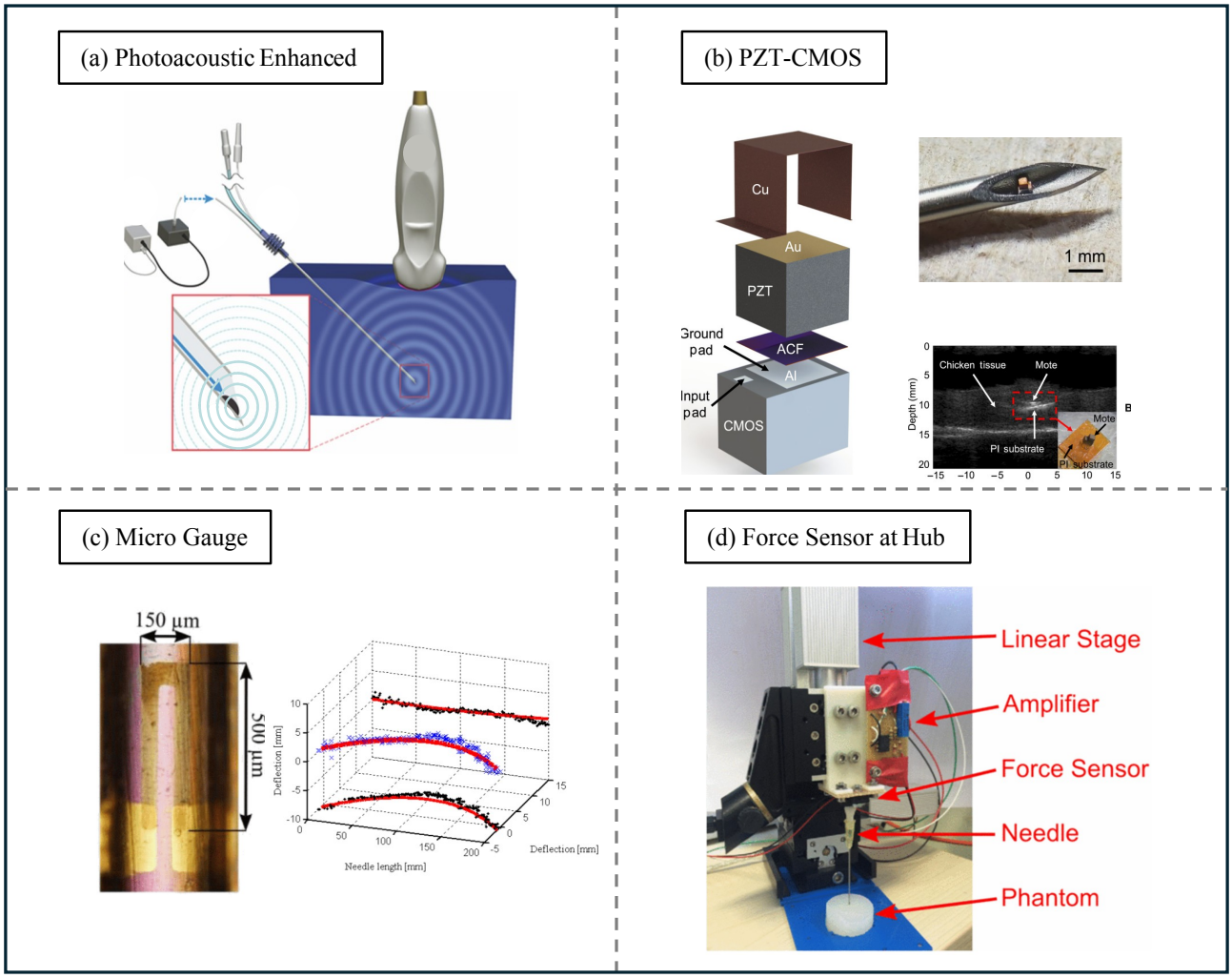

Fig. 2.2. Biomechanical-based needle trajectory guidance techniques. (a) photoacoustic needle tip enhancement using a piezoelectric material [16]; (b) PZT-CMOS passive sensing system [17] (c) mirco strain gauges mounted on the needle shaft for deflection estimation (left) and reconstruction of needle trajectory (right). [18]; (d) hub-based strain sensing incorporating insertion velocity [19].

Studies have aimed to enhance needle tip visibility by attaching materials with distinct acoustic

impedance or by actively generating ultrasound signals at the needle tip through external stimulation. A notable example is the work by Watanabe et al. [16], which employs a photoacoustic approach using a piezoelectric material that emits ultrasound upon light activation. This enhances the needle tip's visibility in ultrasound imaging, as shown in Fig. 2.2(a). Building on Pb-based lead zirconium titanate (PZT), Shi et al. integrated PZT transducers with complementary metal oxide semiconductor (CMOS) circuits to develop an ultrasound probe capable of multiple functions. This system not only enables needle tip localisation but also powers the CMOS and supports the transmission of temperature data [17], as shown in Fig. 2.2(b). However, in certain cases, the generated signal remains difficult to capture or may produce artefacts that create false needle tip images. Moreover, the system requires integration of both optical and ultrasound equipment, along with manual adjustment of imaging parameters such as gain, imposing an additional burden on clinical procedures like CVC. Incidentally, early approaches have also explored the integration of Doppler sensors within the needle structure [20]. When the needle is deployed, the sensor actively emits acoustic waves and captures their echoes. This method has shown particular effectiveness in targeting blood vessels, as the Doppler signal can highlight motion and flow, providing a clear contrast against surrounding static tissues.

Additionally, other studies explored the integration of strain gauges, either mounted directly on the needle shaft or on the hub of the needle luer [18], [19], [21]. For instance, Robert et al. [18] attached micro-gauges to the needle surface, as shown in Fig. 2.2(c). By analysing mechanical strain, a model of needle deflection was reconstructed to estimate the needle's bending direction. The model's predictions were compared with experimental measurements, achieving millimetre-level accuracy. However, the model did not consider certain dynamic factors such as insertion speed. Under more extreme conditions, this led to increased estimation errors.

Building upon this, Zhang et al. [19] relocated the sensors to the needle hub, allowing the incorporation of insertion velocity and tissue viscosity effects into the model, as shown in Fig.

2.2(d). The experimental results demonstrated the effectiveness of this approach. Nevertheless, the study still lacked analysis under multi-angle insertion conditions and across different tissue types, limiting its generalisability in complex clinical scenarios.

Overall, while acoustic impedance-based methods show promise in tracking needle tips, they often require additional equipment, reducing their compatibility with clinical procedures such as CVC. Meanwhile, although mechanically based models have achieved higher accuracy in controlled experiments, their performance remains difficult to validate under the complex and variable conditions present in real human tissue environments.

2.1.2 Optical

Optical methods enable tissue classification through techniques such as optical spectroscopy analysis and Doppler effect measurements. In addition, fibre Bragg (FBG) gratings have also been used to measure needle torque and axial force for needle trajectory guidance.

Cheng et al. [22] proposed a trajectory estimation method using an optical fibre embedded in the needle to project laser onto tissue, with positions calibrated by an electromagnetic tracking system for machine learning training, as shown in Fig. 2.3(a). While effective in controlled settings, the use of external cameras limits its ability to capture in-tissue information during surgery and makes it sensitive to ambient lighting, restricting clinical applicability.

Fig. 2.3(b) shows the external optical markers offer a simple solution for needle tracking, where visual systems can easily identify markers on the needle surface. This approach is particularly advantageous in human-machine interaction (HMI) applications and has been explored in several studies, including work by researchers [23] and commercial implementations such as those by NDI [28]. However, this method has clear limitations—particularly for thin needles—where deformation along the shaft cannot be captured, making it difficult to estimate the actual path.

Diffuse spectroscopy methods identify tissue types by analysing their unique light absorption,

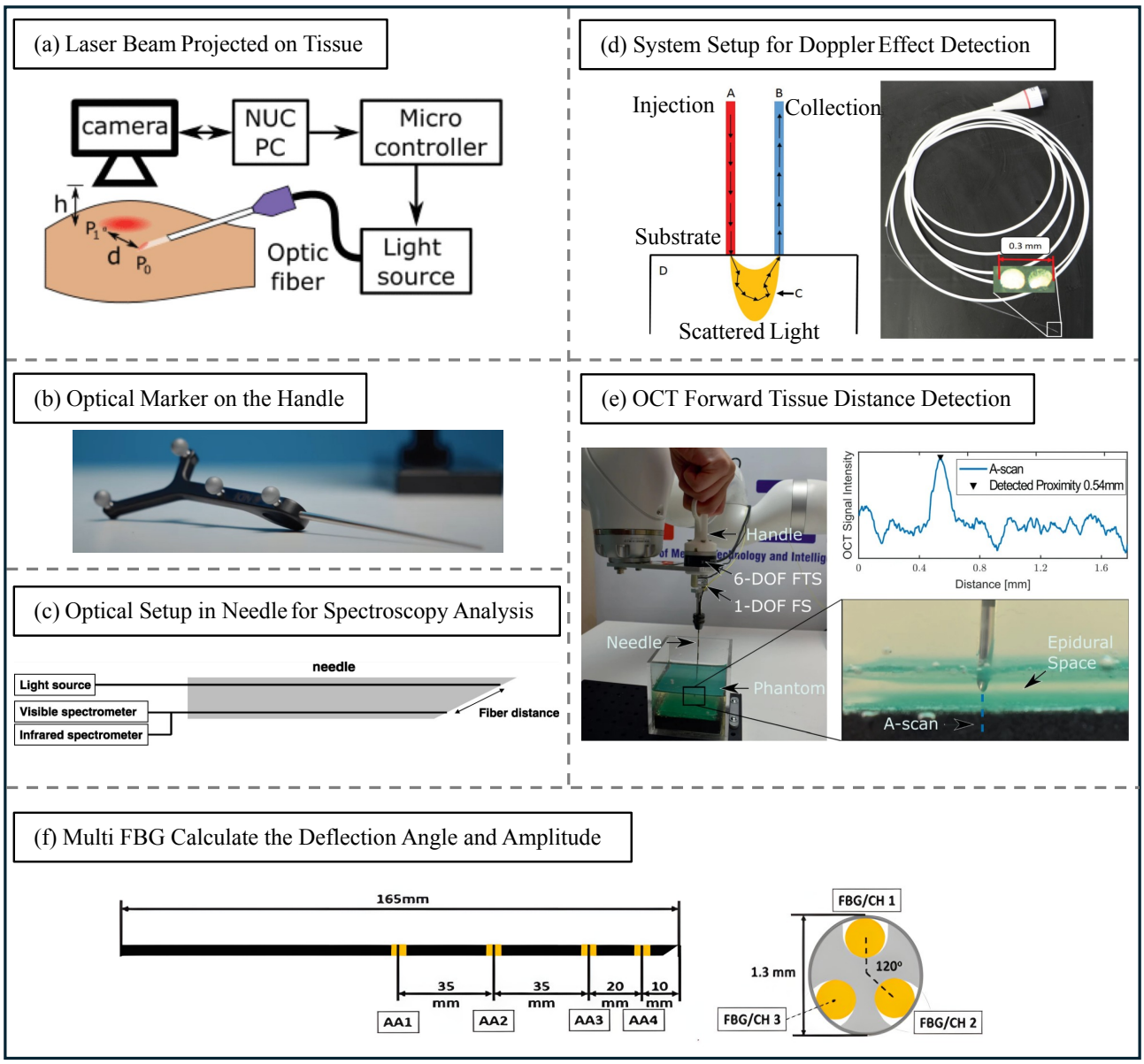

Fig. 2.3. Optical-based tissue classification and needle trajectory guidance techniques. (a) laser beam projected on the tissue surface for trajectory calibration using electromagnetic tracking [22]; (b) external optical markers on the needle handle for visual tracking [23]; (c) integrated optical fibres for diffuse spectroscopy tissue classification [24]; (d) Doppler effect-based system for vascular detection via scattered light [25]; (e) OCT-assisted forward tissue distance detection for precise epidural needle placement [26]; (f) a multi-point FBG array for real-time deflection angle and shape sensing along the needle shaft [27].

reflection, or even emission characteristics. Nachabé et al. [24] developed a needle-integrated system with two optical fibres—one for light emission and the other for detection—to classify health and cancer tissue types in contact with the needle tip, as illustrated in Fig. 2.3(c). While effective in distinguishing spectral features of different tissues, the inclusion of a spectrometer makes the system bulky and limits its potential for miniaturisation.

Another optical approach leverages the Doppler effect, where frequency shifts in light waves occur due to relative motion between the source and the sensor. Virdyawan et al. [25], [29] utilised this scattering-based method to detect blood flow, enabling vascular identification, as shown in Fig. 2.3(d). Although this method allows precise and efficient blood vessel detection, it struggles to differentiate other deep tissue structures such as lymph nodes or nerves. As a result, it lacks the ability to plan a safe insertion path, which may still lead to unintended complications.

Optical coherence tomography (OCT) is a high-resolution imaging technique that, when combined with haptic feedback algorithms, can precisely control needle insertion. In epidural anaesthesia, it has been shown to stop the needle at a distance of 0.21 ± 0.62 mm before puncturing the dura mater, achieving a success rate of 94 % [26]. The complete system is illustrated in Fig. 2.3(e). Despite its precision, OCT has notable limitations. Several studies report that OCT systems are expensive and challenging to integrate into miniaturised instruments [30], [31]. These constraints mirror those faced by acoustic impedance systems, making OCT difficult to incorporate into clinical workflows such as CVC procedures due to its large equipment and high cost.

An array of FBGs can be distributed along the needle shaft to form multiple active sensing regions, with each region containing three FBG sensors arranged 120° apart, as illustrated in Fig. 2.3(f). In the study by Lezcano et al. [27], temperature compensation was considered to minimise the influence of thermal drift on the FBG signal. When the needle bends, the reflected wavelengths from the FBG sensors shift. By analysing the angular deflections and signal amplitudes across multiple active areas and combining these with a mechanical model of the needle, the system can reconstruct its bending details. Further studies have applied machine learning to estimate insertion depth and classify tissue types based on FBG signals [32], [33]. While this method offers high spatial resolution and full needle shape reconstruction, its broader application is limited by factors such as high cost, fragility, sensitivity to temperature changes, and a limited dynamic range [27].

In summary, optical methods for needle tracking offer high precision and valuable insights into tissue

interaction, but each approach faces trade-offs in clinical applicability. Challenges such as system bulkiness, sensitivity to external conditions, high cost, and limited compatibility with miniaturised setups hinder widespread adoption in real-world procedures like CVC.

2.1.3 Magnetic

Compared to optical systems, magnetic tracking devices have made notable progress in miniaturisation. However, most current magnetic tracking implementations still rely on wired connections, which can introduce additional steps and complexity in clinical procedures such as CVC. Despite these limitations, their commercial adoption and research advancements offer valuable insights for future system development.

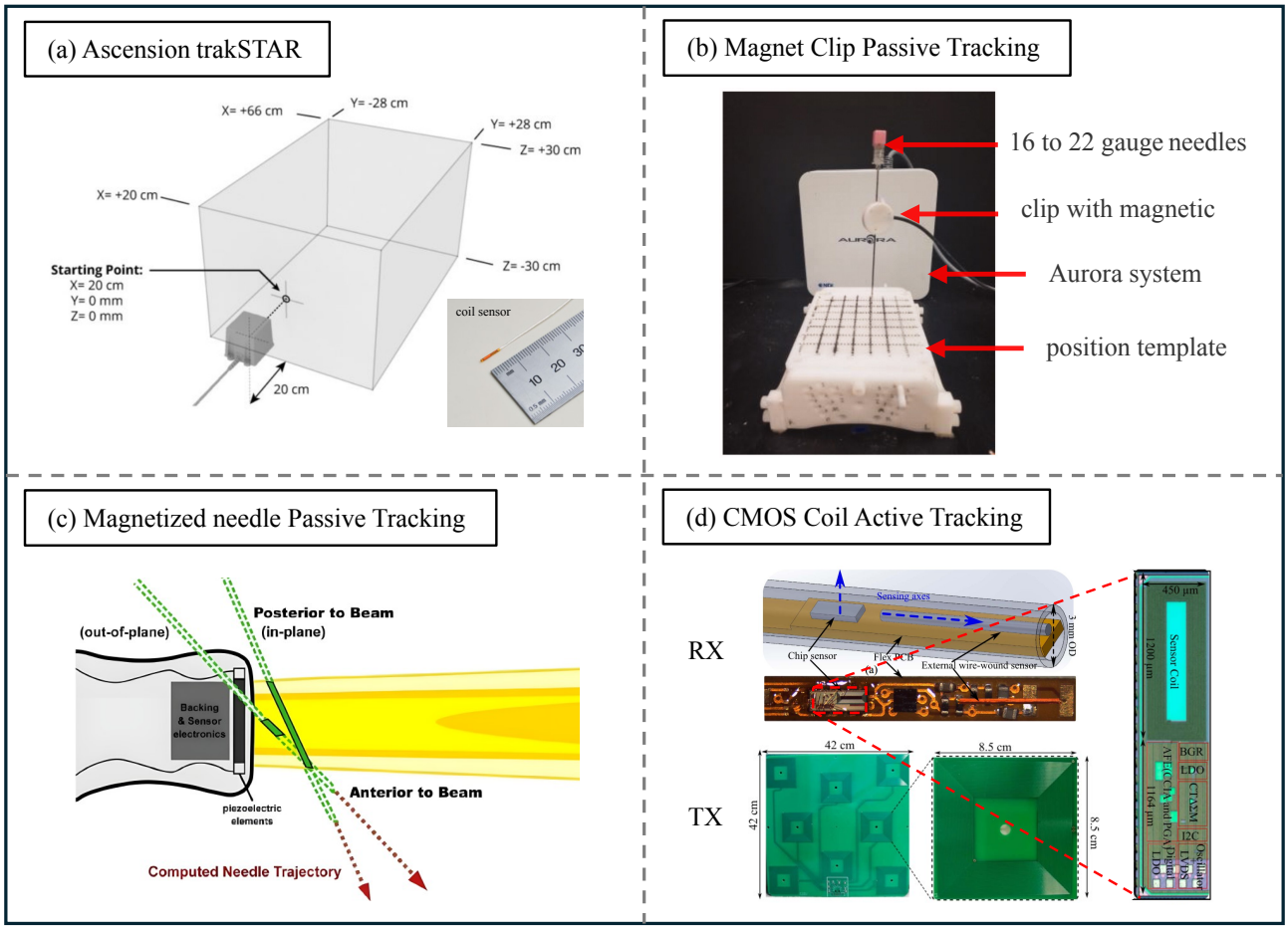

Fig. 2.4. Magnetic-based needle trajectory guidance techniques. (a) Ascension trakSTAR electromagnetic system for 6-DOF pose tracking using a coil sensor [34]; (b) passive tracking using a magnet clip and Aurora field generator for sub-millimetre accuracy [35]; (c) magnetised needle with trajectory overlay on ultrasound for passive guidance [36]; (d) CMOS-based 5-DOF active magnetic tracking system for image-guided bronchoscopy using external coil arrays [37].

Magnetic tracking systems estimate the position and orientation of a needle by analysing the induced currents in miniature coils. One example is the Ascension trakSTAR system, commonly used in medical simulation [34]. It consists of a magnetic field transmitter that emits a low-intensity, time-varying magnetic field. When a microcoil embedded in the tracked object enters this field, it generates an induced current. This signal is then processed by the receiver circuitry to compute the full six degrees of freedom (DOF) pose of the object with 1.4 mm and 0.5 degree root mean square error, as shown in Fig. 2.4(a).

Zhao and Tse [35] proposed a low-cost, disposable needle clip with perpendicular solenoids for 6-DOF tracking using the Aurora field generator, as shown in Fig. 2.4(b). By placing the sensor externally, the design supports various needle sizes and reduces cost, achieving sub-millimetre accuracy. However, performance may be affected by electromagnetic interference and needle bending, and further clinical validation is needed.

Johnson et al. [36] developed a passive magnetic needle guidance system using a magnet at the needle base. It overlays predicted needle trajectories onto ultrasound images, improving targeting accuracy by 57.1 % in phantom studies, as shown in Fig. 2.4(c). Still, precision may be limited by bending and signal errors. Samsung later integrated magnetic sensor arrays into ultrasound probes and used fully magnetised needles for full 6-DOF tracking [38]. While more integrated, it faces similar issues with bending and magnetic interference.

Fig. 2.4(d) shows a 5-DOF magnetic tracking system developed for image-guided bronchoscopy [37]. The system achieves sub-millimetre accuracy within a $15 \times 15 \times 15$ cm^3 volume, using low-frequency magnetic fields generated by an external 8-coil array. Induced signals are digitised by an integrated CMOS sensor to estimate the instrument's pose. While validated against a high-precision optical tracker (NDI Polaris), the system remains limited because of 2D coil configurations, requiring a second coil to enable full 6-DOF tracking. Moreover, it lacks real-time compensation for motion errors caused by respiration or registration drift.

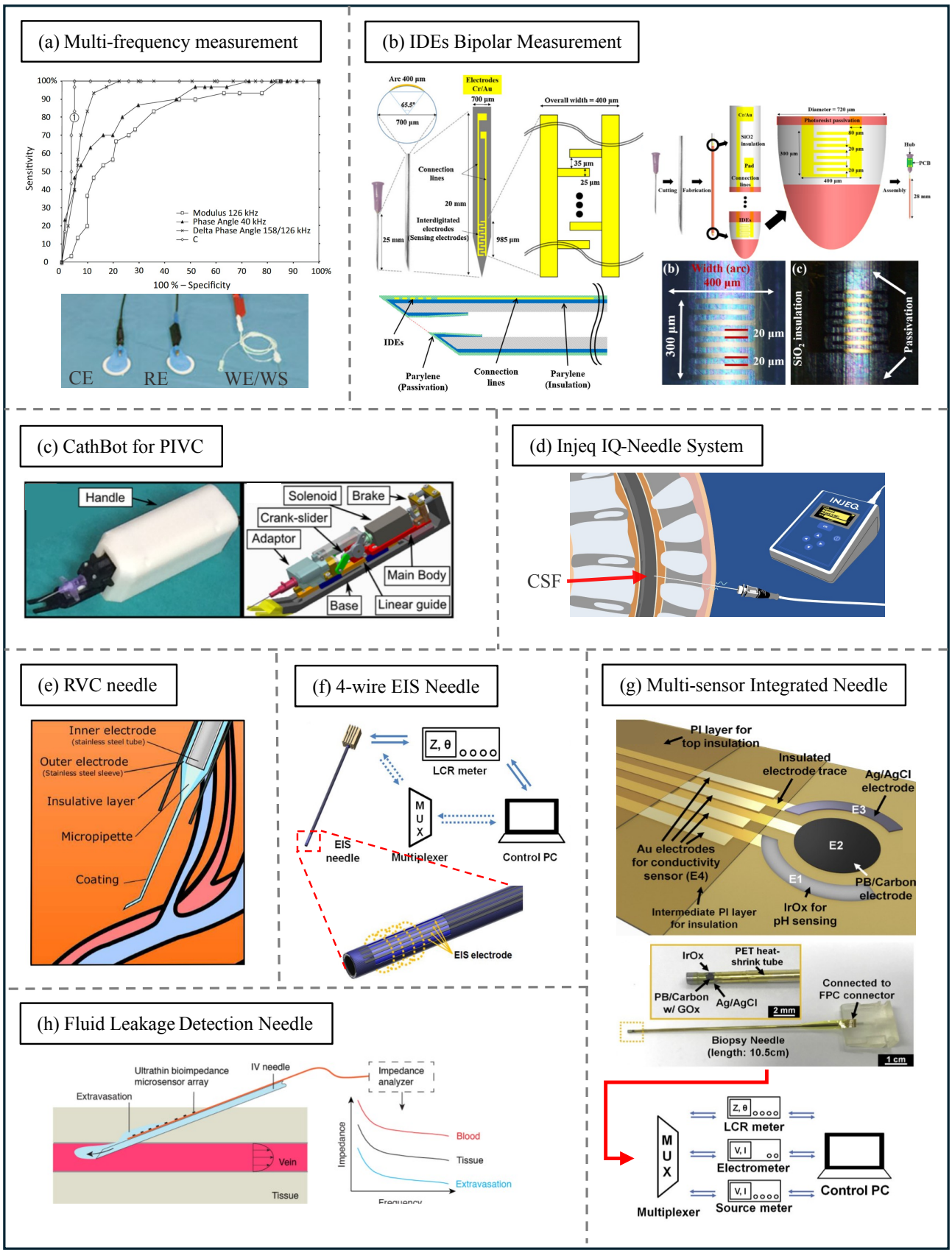

Fig. 2.5. BIOZ-based tissue classification and proximity sensing techniques. (a) multi-frequency for tissue classification [39]; (b) IDE-based bipolar needle for spectral enhancement [40], [41]; (c) CathBot integrating impedance sensing with robotic guidance for PIVC [42]; (d) IQ-Needle for CSF localisation via impedance feedback [43]; (e) two-electrode RVC needle [31]; (f) four-wire EIS needle [44]; (g) multi-sensor needle combining EIS and electrochemical sensing [45]; (h) flexible leakage detection needle with multiplexed impedance readout [46].

2.1.4 Bioimpedance

BIOZ is a highly active area of research, leveraging electrode interfaces for a range of impedances and chemical measurements. Early studies [47]–[49] primarily employed two-electrode or three-electrode configurations to measure tissue impedance. To minimise errors caused by the electrode polarisation effect, later research introduced four-electrode methods for improved accuracy [50], [51]. In addition to impedance measurement, many studies have explored electrochemical sensing using three-electrode configurations and their improved version [51], [52]. The following section provides a detailed review of those developments.

Kalvøy et al. [39] conducted a valuable study in 2016, employing a three-electrode bioimpedance measurement method in which the needle serves as the working electrode, while the other two electrodes are attached to the skin. By incorporating multi-frequency measurements, the discrimination of tissues is improved. For instance, at 40 kHz, the impedance magnitude between nerve and muscle tissues is similar, but the phase response differs significantly. At 126 kHz, the system effectively distinguished between fat and nerve tissue. To enhance classification, an empirical multi-frequency approach was introduced, as shown in Equation 2.1.1, with its performance illustrated in Fig. 2.5(a). Despite its effectiveness, the use of a three-electrode setup introduced drift during repeated measurements due to electrode polarisation effects, which is more fit for the electrochemical measurements. Moreover, the system lacked miniaturisation, and no engineering optimisation was presented, limiting its practical clinical application.

$$C = \sqrt{\left(\frac{-M_{126\text{kHz}} - 73.8 \times P_{40\text{kHz}} - 65.9}{562}\right)^2 + \left(\frac{P_{158\text{kHz}} - P_{126\text{kHz}} + 2.27}{0.95}\right)^2} \tag{2.1.1}$$

Yun et al. [40] developed a bipolar impedance sensing method using fine interdigitated electrodes (IDEs) patterned on the needle tip, enabling tissue discrimination during insertion (Fig. 2.5(b), left). By analysing frequency-dependent spectra and introducing a compensation model for parasitic effects

from the passivation layer, they achieved effective fat–muscle separation at low frequencies (111 Hz). However, unpassivated connection lines introduced high-frequency interference, limiting accuracy.

To address this, a follow-up study applied a selective passivation layer (SPL), exposing only the IDEs (Fig. 2.5(b), right) [41]. This reduced parasitic noise and enabled reliable tissue classification up to 1 MHz. IDEs improve signal quality by increasing electrode–tissue contact and introducing intrinsic capacitance. At high frequencies, their distributed capacitance forms a low-impedance path, allowing current to flow primarily through capacitive coupling rather than resistive conduction. This makes IDEs particularly suited for detecting dielectric properties of tissues. Additionally, their electric field lines are concentrated near the electrode surface, making them sensitive to surface-level interactions.

Many studies have utilised the AD5933 chip (Analogue Devices, USA) combined with commercial or custom-made two-electrode needles for impedance measurements. The limitations of two-electrode configurations—particularly signal drift over time and dominant capacitive effects at low frequencies caused by electrode polarisation—have been discussed extensively. A detailed analysis of these issues will be presented in the next section.

Maglioli et al. [53] applied two-electrode measurements for biological tissue classification. Cheng et al. [42], [54]–[57] combined impedance sensing with mechanical guidance called CathBot to achieve precise peripheral intravenous catheterisation (PIVC), as shown in Fig. 2.5(c).

Some studies employed impedance analysers without considering clinical compatibility or system miniaturisation [30], [31], [58]. Among them, Schoevaerdts et al. [30], [31] focused on retinal vein cannulation (RVC) to treat retinal vein occlusion (RVO), a condition leading to blindness. Similar to CVC procedures, RVC also involves venous puncture. In [31], they used a conventional two-electrode needle but reported a 20 % inaccuracy rate, highlighting challenges for clinical translation, as shown in Fig. 2.5(e). Moreover, the system faced typical limitations associated with bulky external LCR meters and two-electrode drift. Later, Schoevaerdts et al. [30] improved the design by placing the second electrode on the back of the eyeball, enabling early detection of vessel

proximity based on capacitive impedance changes, thus offering better puncture guidance. Helen et al. [58] provided another example where significant system latency caused a mismatch between measured impedance and actual needle position. In contrast, the Injeq IQ-Needle system [43], [59] represents a successful commercial application, achieving precise cerebrospinal fluid (CSF) localisation during lumbar puncture, as shown in Fig. 2.5(d).

Researchers led by Park in Korea have conducted extensive studies on needle design. In earlier work, they developed an EIS-based needle capable of distinguishing tissue types and estimating the location of material interfaces by performing four-wire impedance measurements at two different positions, as shown in Fig. 2.5(f) [44]. Although they demonstrated strong expertise in needle fabrication, their system lacked circuit-level optimisation and full integration, limiting its compatibility with clinical workflows such as biopsy or CVC procedures. In subsequent studies, Park's group integrated electrochemical sensors and four-wire impedance sensors into a single needle design, enabling switching between sensing modes and connecting to multiple instruments for measurement [45], [51]. This multi-sensor integration approach offers valuable insights for future needle system designs, as illustrated in Fig. 2.5(g). Finally, a noteworthy study introduced a flexible printed circuit (FPC) with eight electrodes attached to the needle shaft for early detection of fluid leakage, primarily in PIVC applications [46]. The study also highlighted the use of a PEDOT-MWCNT coating to significantly reduce interface impedance. The system employed a two-electrode measurement method, connecting the eight electrodes to a multiplexer and forming bipolar pairs with a subcutaneous Pt wire, as shown in Fig. 2.5(h). However, it faced similar limitations as previously discussed and will not be elaborated on here.

As mentioned above, many studies have explored electrochemical measurements using electrode-based sensing. However, a detailed analysis is beyond the scope of this research. Representative works can be found in [52], [60], [61]. Compared to other sensing methods, impedance measurement circuits can be efficiently integrated into CMOS technology, offering high portability for applications

in wearable or implantable devices [50], [61]. A more detailed discussion of the electrical models for electrochemical measurements will be provided in the following section.

2.2 Review of the Bioimpedance Technology

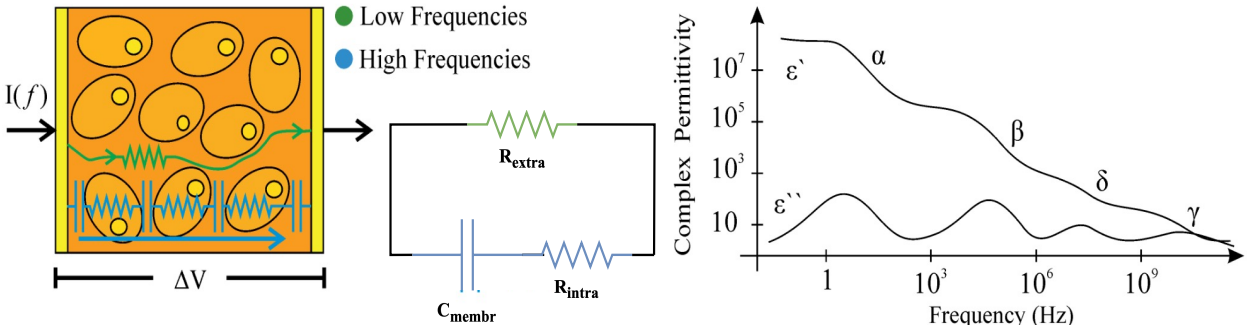

Fig. 2.6. From left to right: (1) Illustration of current pathways at different frequencies through cellular structures [61]; (2) Equivalent circuit model comprising extracellular resistance, membrane capacitance, and intracellular resistance; (3) Frequency-dependent permittivity profile showing α, β, γ, and δ dispersions [62].

The bioimpedance of human tissues primarily arises from the structure of cells and the surrounding tissue matrix. The cell membrane, composed of a phospholipid bilayer, isolates intracellular compounds from the external environment and restricts ion movement. Under the influence of an electric field, ions accumulate at the cell membrane. As the frequency of the applied field increases, ions are unable to follow the rapid field oscillations, resulting in charge accumulation at the membrane and enhanced cell polarisation, thereby facilitating conduction. A basic model of the cell structure is illustrated in Fig. 2.6.

This membrane behaviour can be represented by an equivalent electrical circuit model, where high-frequency signals predominantly probe the conductivity of the intracellular material, while low-frequency signals are more sensitive to the extracellular tissue or interstitial fluid conductivity. As described in [62], [63], biological tissues exhibit characteristic impedance responses across different frequency bands, commonly referred to as the α, β, γ, and δ dispersions. Notably, the characteristic frequency for different tissues falls within the α and β bands, typically in the range of

0–100 kHz. This frequency range forms the basis for the sensing strategy adopted in later work aimed at differentiating tissue types during CVC procedures.

Before conducting finite element method (FEM) simulations of needle insertion into biological tissues, it is essential to understand several key factors. These include the intrinsic properties of biological tissues (as previously introduced), the contact characteristics between electrodes and tissue, and the equivalent circuit models representing this interface.

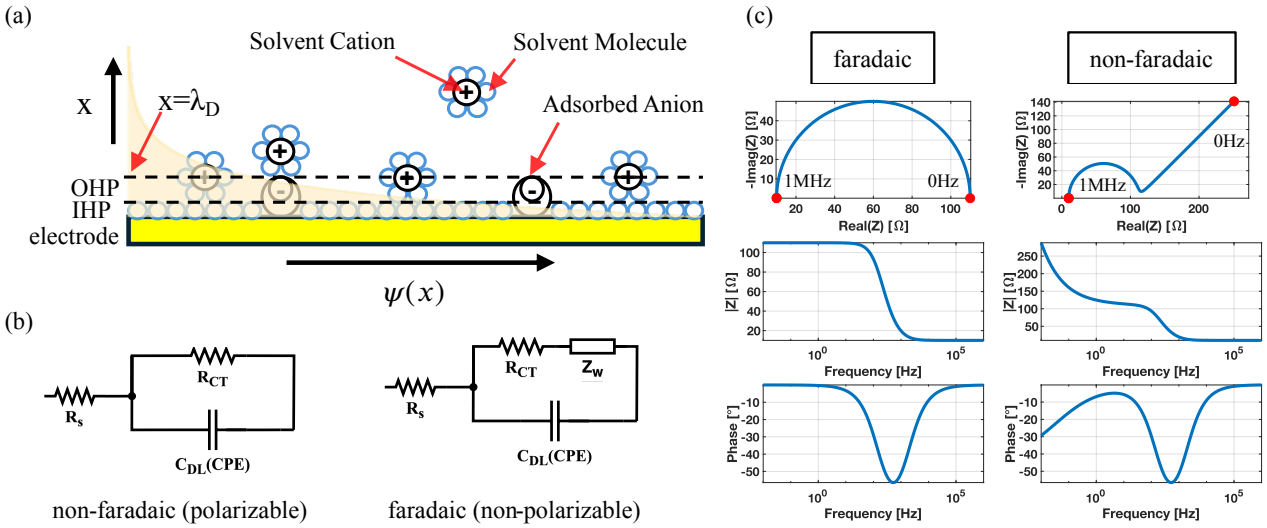

Fig. 2.7. Electrode–Tissue Interface and Equivalent Circuit Models. (a) Schematic of the electrode–solution interface showing the inner and outer Helmholtz planes. (b) Equivalent circuit models for non-Faradaic and Faradaic electrodes, including DLC charge transfer resistance and Warburg impedance. (c) Representative impedance spectra for faradaic and non-faradaic electrodes: Nyquist plots (top), impedance magnitude (middle), and phase angle (bottom) versus frequency.

Specifically, when electrodes come into contact with a solution or tissue environment, electrode polarisation effects occur, as illustrated in Fig. 2.7(a). The first layer formed on the electrode surface consists of specifically adsorbed small ions (e.g., H^+, Cl^-) and water molecules, known as the inner Helmholtz plane (IHP). This is primarily composed of water molecules due to their strong dipole moment. The second layer, referred to as the outer Helmholtz plane (OHP), consists of hydrated ions attracted by the electric field. Together, these two layers form capacitive structures that effectively shield the electrode's electric field, causing a sharp decay in the field strength beyond this region. Consequently, the electrode's sensitivity to external chemical reactions or tissue conductivity changes is significantly reduced.

It is worth noting that some studies have introduced large molecules such as polyethylene glycol (PEG) onto the electrode surface [64]. These molecules do not participate in electric field shielding but effectively prevent additional hydration layers from forming, thereby expanding the sensitive region and improving electrochemical impedance measurements.

Overall, the characteristic thickness of this double-layer capacitance (DLC) region is referred to as the Debye length, defined by Equation 2.2.1.

$$\lambda_D = \sqrt{\frac{\varepsilon_r \varepsilon_0 k_B T}{2 N_A e^2 I}} \tag{2.2.1}$$

where λ_D is the Debye length, ε_r is the relative permittivity of the electrolyte, ε_0 is the vacuum permittivity, k_B is the Boltzmann constant, T is the absolute temperature, N_A is Avogadro's number, e is the elementary charge, and I is the ionic strength of the solution which is described by the equation below:

$$I = \frac{1}{2} \sum_i c_i z_i^2 \tag{2.2.2}$$

In this expression, I is the ionic strength of the solution (in mol/L), c_i is the concentration of ion species i, and z_i is the valence (charge) of ion species i. The Debye length primarily depends on the ionic strength of the solution surrounding the electrode. Under physiological conditions, the thickness of the electrical double layer is typically less than 1 nm.

The DLC effect described above is represented in the equivalent circuit as C_{DL}, as shown in Fig. 2.7(b). The circuit also includes R_{CT}, which reflects the resistance associated with electron and ion exchange at the electrode interface, and R_S, representing the bulk resistance of the solution.

Electrodes can be classified into two types. The first type, non-Faradaic or polarisable electrodes, exhibit a very large R_{CT}, effectively preventing charge transfer across the interface. In this case, only displacement currents are generated, relying purely on the electric field. Some studies have sought to

further reduce R_{CT} by increasing the electrode–tissue contact area [65], thereby enhancing the DLC and improving displacement current conduction. This reduction in interfacial impedance improves the accuracy and quality of the measured signal by better preserving the contribution from R_S.

The second type, faradaic or non-polarisable electrodes, allows redox reactions at the electrode surface, facilitating electron and ion exchange and resulting in a relatively small R_{CT}. In faradaic electrodes, the influence of Warburg impedance at low frequencies must also be considered. Its equation is given as follows:

$$Z_W = \frac{\sigma}{\sqrt{\omega}}(1-j) \tag{2.2.3}$$

where σ is the Warburg coefficient, which is related to the diffusion coefficient and concentration gradient and ω is the angular frequency. Therefore, at low frequencies, the impedance exhibits an inverse relationship with frequency. The typical impedance responses of these equivalent circuits are illustrated in Fig. 2.7(c).

Additionally, the choice of electrode configuration—such as the number and arrangement of electrodes—directly affects the measurement method, each with its respective advantages and limitations. It is also important to establish appropriate system evaluation metrics. These include electrode sensitivity analysis, the relationship between impedance measurements and electrode spatial positioning, and error analysis. To support these analyses, it is essential to first define the basic impedance measurement model. In general, impedance $Z(f)$ at a given frequency f can be expressed as

$$Z(f) = R + jX = \frac{V_o \sin(2\pi ft + \phi)}{I_o \sin(2\pi ft)} \tag{2.2.4}$$

where V_o and I_o are the amplitudes of the voltage and current signals, respectively, and ϕ represents the phase difference between them. This relationship forms the basis for interpreting the electrical

properties of the system under different electrode configurations. Therefore, the following subsections will systematically analyse different system characteristics and evaluation indicators based on electrode setup considerations.

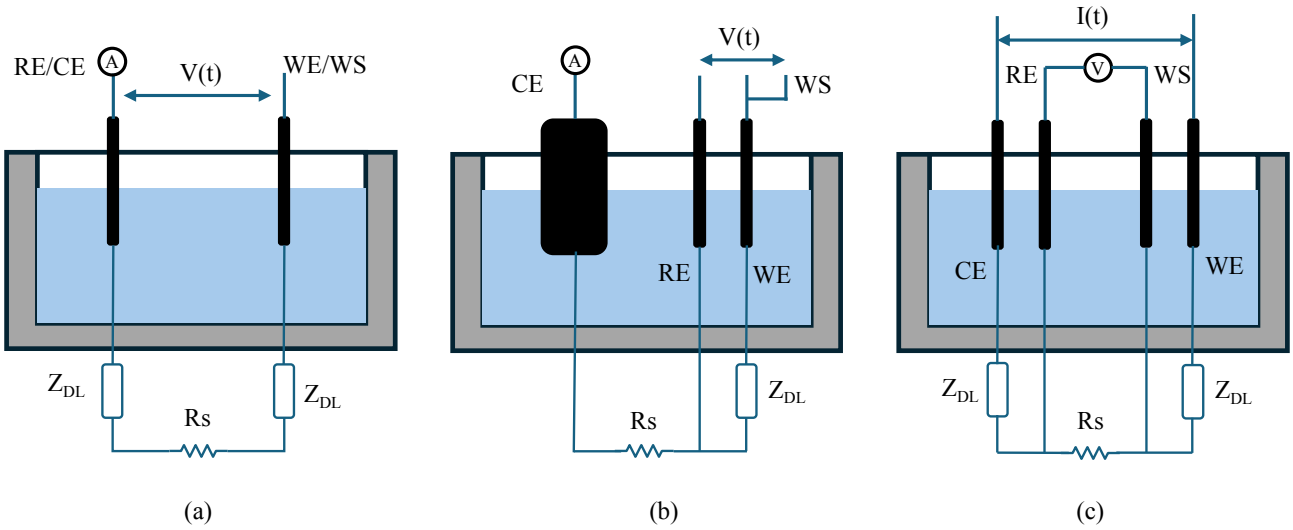

Fig. 2.8. Comparison of two-, three-, and four-electrode configurations for impedance measurements.

2.2.1 Bipolar

The drawbacks of bipolar electrode configurations have been repeatedly discussed in the previous reviews, primarily due to the significant measurement errors and drift caused by DLC effects. The corresponding equivalent circuit is shown in Fig. 2.8(a), where Z_{DL} represents the impedance introduced by the DLC, which critically impacts measurement accuracy. The sensitivity of the bipolar system can be expressed by the following equation:

$$S_{\text{bipolar}} = \frac{J_x^2 + J_y^2 + J_z^2}{I^2} \tag{2.2.5}$$

where J_x, J_y, and J_z are the current density components in the x, y, and z directions, respectively, and I is the total injected current. The depth of investigation (DOI) is defined as the region through which the majority of the current flows. DOI is linearly dependent on the electrode spacing, but it is insensitive to the electrode width [66].

2.2.2 Tripolar

The three-electrode configuration is commonly used for measurements at the electrode surface, where specific antibodies or biomolecules are immobilised to enable impedance-based detection of biochemical reactions, indirectly verifying the presence of a target analyte, as shown in Fig. 2.8(b). As mentioned earlier, Park et al. integrated glucose and pH sensors into a biopsy needle, using a multi-modal sensor array to enhance the accuracy of image-guided biopsy procedures [51]. In three-electrode designs, the counter electrode (CE) typically has a larger contact area than the working electrode (WE), effectively reducing DLC effects at the CE in order to focus the surface impedance changes on the WE. The reference electrode (RE) is placed close to the working electrode (WE) to precisely control the WE potential. Additionally, a working source (WS) electrode is connected to apply a voltage source between the WS and RE, enabling controlled stimulation of the WE. Some studies have introduced interdigitated capacitive structures to confine over 90% of the electric field within a $5\mu m$ region, improving sensitivity to small biological targets such as bacteria [67].

Research in this area primarily focuses on optimising electrode structures and surface modifications to better match the detection space with specific biochemical applications.

2.2.3 Tetrapolar

The four-electrode (tetrapolar) method effectively bypasses the capacitive effects introduced by the DLC, enabling direct measurement of the solution impedance, which is the primary target in this study. Although the interface impedance does not directly affect the measured value, it still imposes a significant load on the current source. Therefore, the current source must maintain a sufficiently large output voltage swing to ensure stable current injection, which requires careful circuit design considerations.

In a four-electrode setup, the current is injected through the current electrodes, creating an electric

field in the solution, while the voltage electrodes measure the local potential difference. The size of the electrodes influences the measured solution impedance. Smaller electrodes result in a concentrated current injection region, causing the current to rapidly spread into the surrounding medium. Consequently, the effective current path volume becomes smaller, leading to an increase in the measured resistance. Moreover, when using small electrodes, the sensitivity region becomes highly localised and concentrated. This produces higher electric field gradients, meaning the measured conductivity tends to represent more local values rather than the bulk average. While the decrease of electrode size would increase the impedance difference between different solutions, which enhances the relative signal-to-noise ratio (SNR) against system noise, it also introduces additional thermal noise, potentially influencing the overall SNR performance. The sensitivity distribution for a four-electrode configuration can be described by the following equation:

$$S_{\text{tetrapolar}} = \frac{\mathbf{J}_1 \cdot \mathbf{J}_2}{I_1 I_2} \tag{2.2.6}$$

where $\mathbf{J}_1$ is the current density vector resulting from the injection through one pair of electrodes, and $\mathbf{J}_2$ is the current density vector obtained by exchanging the injection and measurement electrode pairs. The sensitivity distribution is then computed based on the interaction of these two current fields. The DOI is strongly dependent on the electrode setup and can be approximated by the following expression:

$$z_{\text{median}} = \frac{1}{2}\sqrt{\left(\frac{D_1}{2} + D_2\right)^2 - \left(\frac{D_1}{2}\right)^2} \tag{2.2.7}$$

where D_1 is the spacing between the current injection electrodes, and D_2 is the spacing between the voltage measurement electrodes.

2.3 BIOZ Circuits

An impedance measurement system typically consists of two main components. The first is the analogue front-end (AFE), which includes a voltage-excitation or current-driving circuit, along with a voltage readout circuit. The second component is the impedance demodulation and control unit, which extracts the magnitude and phase of the target impedance. It also manages system configuration through programmable control of parameters such as gain, injection current, and frequency while supporting flexible switching between various demodulation schemes. Whether implemented using discrete components or fully integrated through CMOS technology, such systems can be significantly miniaturised, making them highly suitable for wearable or implantable medical devices.

2.3.1 Voltage Excitation

There are various methods for generating voltage excitation signals in impedance measurement systems. Common approaches include using lookup tables with pre-stored sine waves driven by an MCU or FPGA or directly employing a direct digital synthesis (DDS) module. In contrast to digital waveform synthesis, analogue signal shaping can be achieved by exploiting CMOS devices operating in the subthreshold, which exhibit an exponential current-voltage relationship due to diffusion-dominated conduction. This exponential characteristic allows a triangular input signal to produce an output waveform that approximates a sine wave [68].The circuits in Fig. 2.9(a) shown in the image leverage this property of CMOS transistors in the subthreshold region. For applications requiring chirp signals, a voltage-controlled oscillator (VCO) offers a practical and compact solution , as it allows the output frequency to be modulated by a control voltage input. The circuit demonstrates how this can be implemented efficiently by exploiting the subthreshold characteristics of CMOS devices to achieve both waveform conversion and frequency control in a single design.

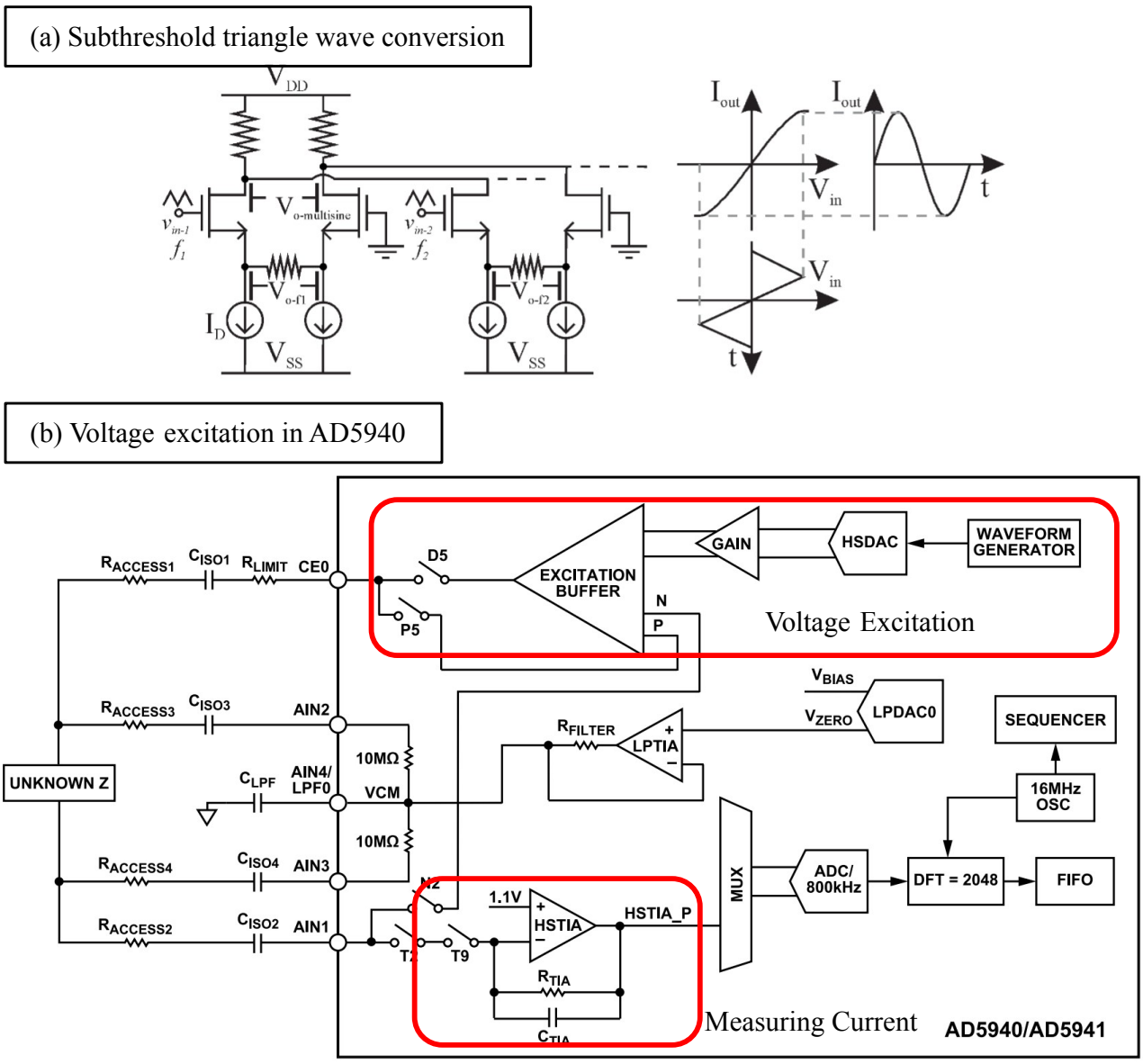

Fig. 2.9. Voltage Excitation Methods for Impedance Measurement. (a) Subthreshold CMOS triangle-to-sine converter [68]. (b) AD5940 integrated excitation system with DAC and output buffer stages [69].

A representative example of a voltage-excitation system is the AD5940 by Analogue Devices [69], as shown in Fig. 2.9(b). It employs a high-speed digital-to-analogue converter (DAC), followed by amplification and filtering stages, and concludes with a differential-output buffer (DDTA) to generate accurate voltage signals. Since voltage is injected into the system, a transimpedance amplifier (TIA) is used in the return path to measure the resulting current. This allows precise current sensing, which is essential for subsequent impedance reconstruction.

It is important to consider signal quality during excitation, particularly the SNR. Signals that have a

high crest factor (CF), which looks at the peak of the signal compared to its average value, can show a high SNR but are also more likely to get distorted in a nonlinear way. Excessive CF can lead to clipping and harmonic distortion, introducing spurious components into the impedance measurement. Moreover, the excitation current must remain within medically safe limits to comply with IEC 60601 standards and ensure patient safety.

2.3.2 Current Driving

The voltage excitation circuit mentioned above follows the IEC 60601 safety standards. To meet these requirements, a series current-limiting resistor is added to ensure the injected current remains within safe limits. Additionally, coupling capacitors are used to block any DC components from entering the body. Similarly, when designing current sources, it is important to consider the safety limits for injected current. The maximum allowable current is defined by the following equation [50], [61]:

$$I = \begin{cases} 100\mu \text{ A}_{\text{rms}} & 0.1 \text{ Hz} < f < 1\text{kHz} \\ 100\frac{f}{1\text{kHz}}\mu \text{ A}_{\text{rms}} & 1\text{kHz} < f < 100\text{kHz} \\ 10 \text{ mA}_{\text{rms}} & 100\text{kHz} < f \end{cases} \tag{2.3.1}$$

Compared to voltage excitation, the design of current sources is generally more complex. When driving high-impedance loads, the stability of the output current may degrade, leading to inaccurate impedance measurements. In a four-electrode configuration, although electrode polarisation effects within the measurement region can be neglected, these effects remain significant at the current-injecting electrodes. The additional impedance introduced by polarisation cannot be ignored and must be carefully considered during current source design. This requires the current source to exhibit a high enough output impedance and sufficient load-driving capability.

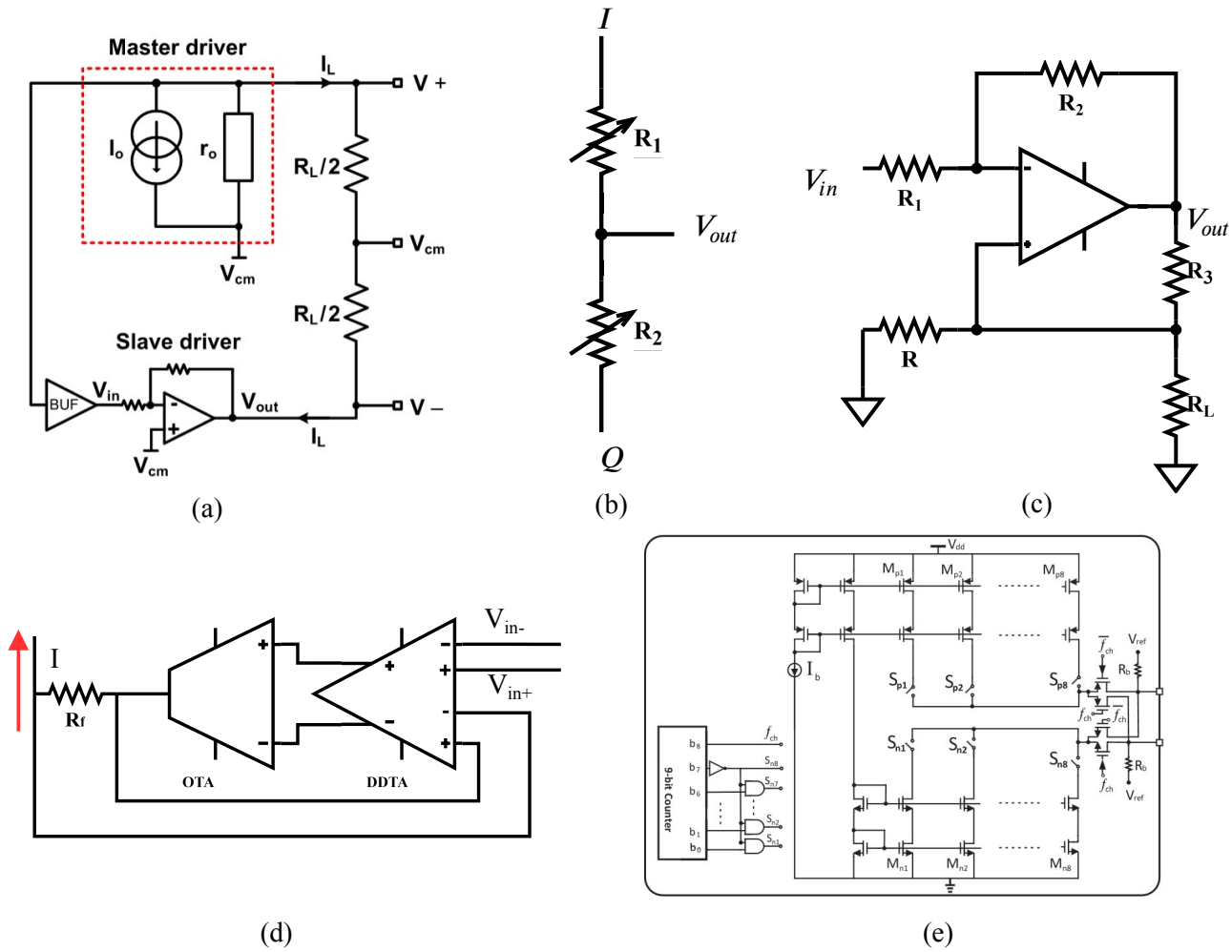

Fig. 2.10. (a) Differential master–slave driver with common-mode feedback [70]. (b) Feedforward-compensated dual-transconductance driver [71]. (c) Howland current source. (d) DDTA enhanced OTA-based current source [72]. (f) DAC-Based open-drain bidirectional current driver [73]

Another important consideration is the improvement of common-mode rejection. As noted in [50], differential current sources offer significantly better common-mode interference suppression compared to single-ended designs. However, achieving perfect symmetry in differential current sources is challenging in practice. Mismatch between the source and sink paths can result in a portion of the current leaking through the high output impedance path to ground, generating excessive common-mode voltage. This may saturate the front-end circuitry and prevent accurate signal acquisition. To address this issue, the circuit shown in Fig. 2.10(a) employs a master-slave architecture with common-mode feedback (CMFB) [70]. The slave stage uses an inverting amplifier referenced to the common-mode voltage (V_{CM}), which dynamically adjusts the sink voltage to match the source voltage. Specifically, when the open-loop gain of the inverting amplifier at the slave side

is set to 1, the two voltages are symmetrically distributed around V_{CM}. With identical load resistances, current conservation is maintained between the source and sink terminals. It is important to note that this current matching is valid only when r_o is much greater than the load resistance. Under this condition, the current flowing through the load can be approximated as the input current of the current source, enabling proper current matching through common-mode feedback.

Generally, there are two types of current drivers, including the voltage-controlled current sources (VCCS) and the DAC-based open-drain current mirror. For VCCS, ideally it should have infinite output voltage compliance and infinite output voltage impedance throughout the bandwidth and no nonlinearities. In integrated designs, various types of current drivers have been developed [72], [74]. Actually, except for the source and sink mismatch problem mentioned before. If the output impedance is not high enough compared to the load, the harmonic components severely degrade the accuracy of impedance spectra. Additionally, due to internal parasitic capacitance and other non-idealities, VCCS implementations often introduce phase delay, affecting the accuracy of phase measurements [61]. To address these issues, several circuits have been proposed. For instance, feedforward compensation architectures employ dual transconductance stages to generate quadrature signals, which minimised the phase error of the output current, as shown in Fig. 2.10(b). Although they can effectively suppress phase distortion of the injection current, these approaches lack closed-loop control [71]. In discrete implementations, the Howland current source and its enhanced variants remain widely used for constructing VCCSs in impedance measurement and bioelectric stimulation systems, as shown in Fig. 2.10(c). A notable circuit design involves feeding the differential signal from the DAC into a DDTA. At the output stage, a feedback resistor converts the output current back into a voltage, which is the feedback path to the DDTA. This configuration ensures that the voltage difference across the resistor matches the input voltage, thereby maintaining a constant output current regardless of load variations [72]. Compared to a single-ended operational transconductance amplifier (OTA), this design significantly improves load-driving capability, as

shown in Fig. 2.10(d). Similarly, in order to improve the OTA stage's current load capacity, [75] used a common class AB buffer to provide a push-pull output.

For the DAC-based open-drain current mirror, shown in Fig. 2.10(e), an N-bit binary-weighted array of PMOS (source) and NMOS (sink) mirrors is gated by a digital control word to realise a programmable bidirectional current source. Because each branch is connected in open-drain configuration, the output node remains high-impedance and can swing over almost the full supply range, granting large voltage compliance [73]. The digitally selectable mirror halves provide fine amplitude resolution, while intrinsic device matching and cascode stacking keep the output resistance high enough that the delivered current is practically insensitive to load variations.

2.3.3 Voltage Readout

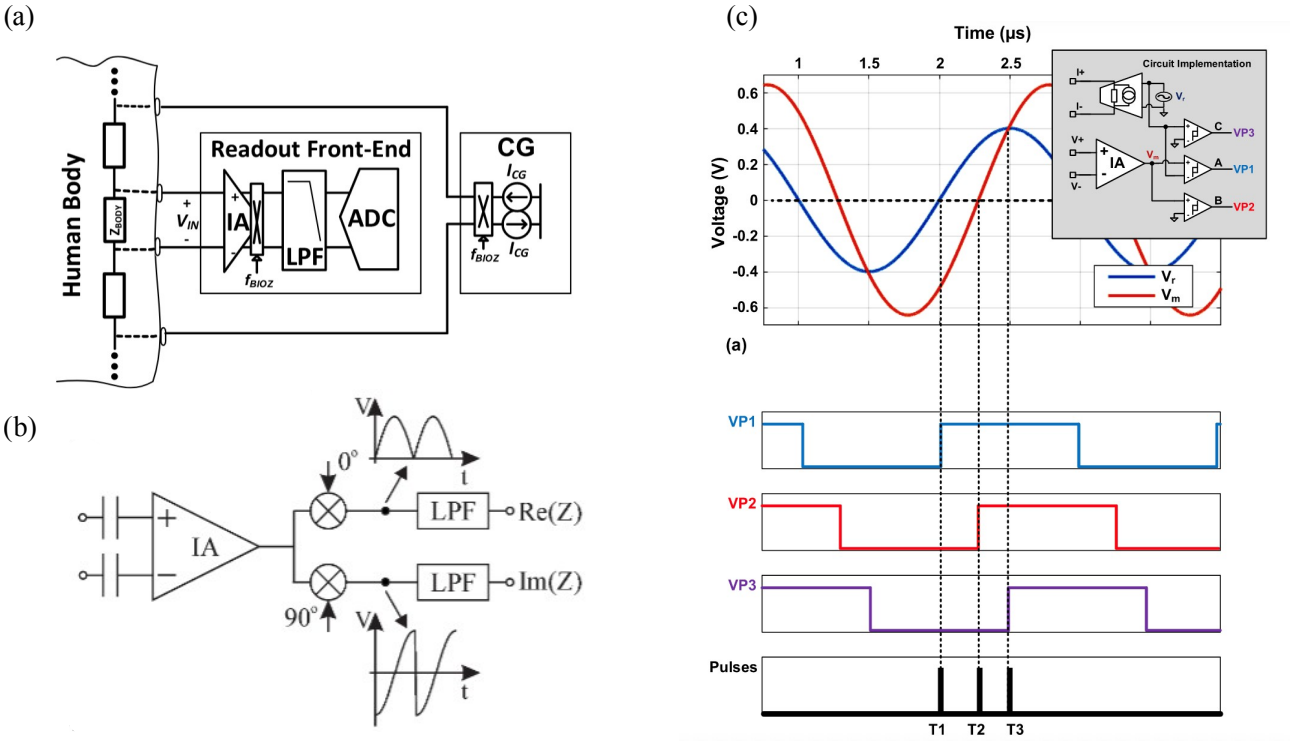

Fig. 2.11. (a) IA voltage readout circuit using choppers to reduce 1/f noise [76]. (b) IQ demodulation [77]. (c) Time stamp demodulation [78].

The design of an instrumentation amplifier (IA) should trade off common mode rejection ratio (CMRR) and linear range. A high CMRR is essential to suppress common-mode noise caused by

power supply fluctuations or electrode interference. Meanwhile, a wide linear range is crucial to accommodate the large variations in tissue impedance. If the measured signals fall outside the IA's linear operating range, measurement distortion may occur.

In addition, a high SNR is critical for sensitivity. Theoretically, in needle-based impedance measurement systems, changes in conductivity at greater tissue depths can cause variations in the measured impedance. However, due to the small sensitivity region of needle electrodes, these changes are often difficult to detect. A high-SNR detection system can effectively capture such deep conductivity changes, enabling impedance-based proximity detection of blood vessels as the needle approaches. To achieve this, chopper-stabilised instrumentation amplifiers (IAs) are commonly used for voltage readout of target tissues. These amplifiers offer ultra-low noise performance and fine resolution (<0.1 Ω) [76], [79]. A typical measurement configuration is shown in Fig. 2.11(a) [76], where the input signal is modulated and subsequently demodulated at the output stage. This modulation process shifts low-frequency noise components (primarily 1/f noise) to higher harmonics. By applying a bandpass filter during demodulation, out-of-band noise is effectively removed, significantly reducing noise energy. Before the source signal goes into the IA, buffers are needed to isolate the measurement. In addition, the feedback circuits in IA circuits could be categorised into current feedback and voltage feedback. Current feedback achieves a higher CMRR but at the cost of increased power consumption. In contrast, voltage feedback provides better linearity with lower power consumption, making it suitable for low-power applications. The IA circuit is typically followed by a demodulation stage, which extracts the amplitude and phase information of the impedance signal directly. Below, several demodulation strategies are introduced. The first method involves sampling the output signal of the IA using an analogue-to-digital converter (ADC), which then sends the digital samples to an FPGA or MCU for processing. In this approach, the input signal is multiplied by two orthogonal reference signals. By applying low-pass filtering to the results, the in-phase component (I) and quadrature component (Q) are obtained, representing the

amplitude and phase information, respectively. After one complete single cycle, the accurate amplitude and phase information can be extracted. It is important to note that the sampling rate of the ADC must be sufficiently high to ensure adequate resolution and data points for precise reconstruction, as illustrated in Fig. 2.11(b). This method involves a trade-off between SNR and demodulation speed. Consequently, various demodulation techniques have been developed to enhance both accuracy and speed simultaneously [50], [80]. Another approach converts the amplitude information to the time domain. This method employs three comparators to detect the zero-crossings of the original input signal, the IA output signal, and the crossing points between the two signals. A high-frequency counter is used to measure the time intervals between these crossings. The counter values are then used to compute the phase and amplitude of the current signal [78], as shown in 2.11(c).

2.4 Robotic-assisted Medical Procedures

A complete system comprises not only multi-sensing technologies and fine circuit designs described earlier but also automated or auxiliary mechanical structures. Manual operation alone cannot establish a closed-loop control with the sensing module, which is crucial for real-time feedback and precise needle positioning. The following sections introduce active and auxiliary multi-sensor integrated systems designed to enhance the needle insertion process.

2.4.1 Automated Robotic Systems

Robotic venipuncture systems have been developed to improve accuracy and reduce human error in venous access, particularly for patients with difficult venous access (DVA). Balter et al. [81] expanded the venipuncture system to a 9-DOF configuration, integrating stereo vision for 3D mapping, US imaging with Doppler capabilities, and enhanced force sensing (FS). The 6-DOF gantry and 3-DOF needle manipulator allowed for improved spatial freedom and adaptive kinematic

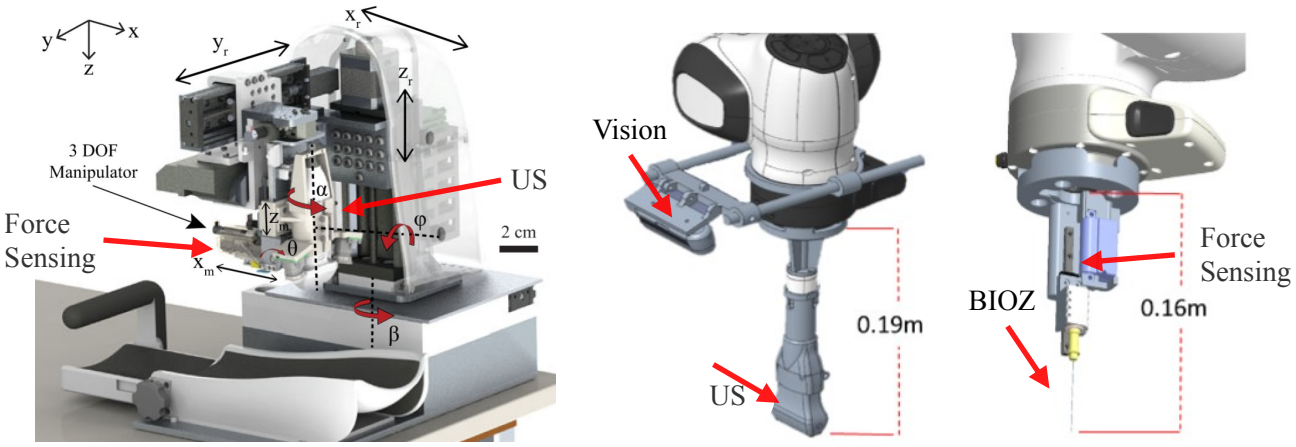

(a) (b)

Fig. 2.12. (a) 9-DOF PIVC automatic robotic system [81]. (b) dual robotic arm system for CVC [82].

control. Stereo vision enabled 3D vessel mapping and dynamic tracking, overcoming NIR's depth limitations. Phantom studies reported a positioning accuracy of 0.22 ± 0.05 mm, and US-guided tracking achieved 0.004 mm error at 0.5 mm/s and 0.8 mm at 10 mm/s. The enhanced visual servoing also allowed real-time adjustments to needle trajectory, increasing robustness against vessel movement, as shown in Fig. 2.12(a). In addition, the CathBot mentioned in Fig. 2.5(c) is a system that uses BIOZ for detection and then combines a mechanical structure for needle insertion. Both of them are PIVC application systems for PIVC [42]. Koskinopoulou et al. [82] introduced a fully autonomous dual-robot collaborative system for CVC, including US, BIOZ, 3D vision, and FS. The system consists of two Franka robotic arms: one for US scanning and vessel segmentation and the other for needle insertion with real-time BIOZ monitoring, as shown in Fig. 2.12(b). Experimental results demonstrated an average RMS error of 1.71 mm during autonomous venipuncture, with high accuracy in vessel detection. The dual-arm collaboration allows simultaneous scanning and insertion, reducing misalignment risks and improving targeting for deep veins, making it suitable for CVC procedures. However, the size limitation of the dual robotic arms has limited access to practical medical procedures.

Although the aforementioned fully automated robotic systems achieve high precision, their size and fully autonomous operation often lead to patient discomfort and trust issues [83]–[85]. In contrast,

robot-assisted procedures with clinician involvement are generally more acceptable to patients.

2.4.2 Auxiliary Robotic Systems

To address this gap, auxiliary robotic systems have been proposed. Leipheimer et al. [86] presented a hand-held robotic venipuncture device integrating 2D US imaging, miniaturised robotics, FS, and an electromagnetic (EM) sensing needle loader for peripheral venous access. The device achieved an 87% success rate across 31 participants, with 97% success in non-DVA cases, highlighting its potential in routine blood draws. The system employs ultrasound for vessel localisation, an inline force sensor for insertion feedback, and an electromagnetic mechanism for precise needle handling. The reported needle placement accuracy was 0.23 ± 0.17 mm, demonstrating high precision in peripheral vein targeting. However, the hand-held design requires completely manual positioning and alignment, and its structure limits the application for deeper venous targets. This lack of haptic feedback makes it difficult for the operator to maintain precision during insertion, which has led to the exploration of haptic technologies to enhance manual control and feedback during medical procedures. Mieling et al. [87] introduced a collaborative robotic biopsy system combining trajectory guidance and needle tip force feedback with a 7-DOF KUKA LBR Med 14. It integrates OCT and machine learning for real-time force sensing. Phantom studies showed 91% detection accuracy for tissue interfaces, with 5.45 ± 3.31 mm for entry and 9.85 ± 4.89 mm for exit. Despite its effectiveness, the size of the system limits practical use.

Quesada et al. [88] presented a haptic simulator focused on tissue tearing during laparoscopic surgery. The system leverages a real-time interactive environment to simulate tissue damage with force feedback, achieving high responsiveness with a feedback rate of 1 kHz. This simulator enhances the tactile experience for surgeons during training, allowing realistic interaction with tissue layers. Ríos-Hernández et al. [89] developed a haptic-based lumbar puncture simulator for medical training. The system integrates virtual reality with force feedback to simulate needle insertion

through lumbar tissues, enhancing realism and improving student confidence. The simulator incorporates real-time tissue deformation and sensory feedback, aiming to reduce error rates during clinical procedures. Ravali and Manivannan [90] reviewed haptic feedback technologies for needle insertion simulation. Their study highlighted 6-DOF force feedback for simulating friction, cutting, and tissue resistance. Classical models like FEM and spring-damper were evaluated for real-time simulation, demonstrating improved spatial awareness and insertion precision. Haptic has been of great help in medical simulation and teaching, but although it has great potential in real-time medical surgery, it still has a long way to go. [91] is a successful commercial case, as illustrated in Fig. 2.13.

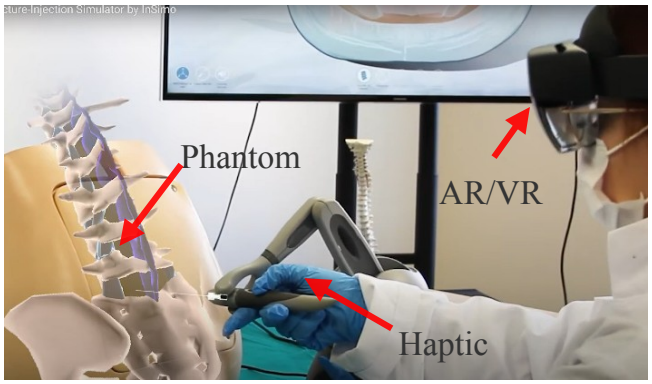

Fig. 2.13. InSimo haptic tutorial case.

The following will compare the performance parameters of those multi-sensor systems, as shown in Table 2.1. The last column refers to previous work, which will be discussed in detail in the next chapter.

Table. 2.1. Performance Summary and Comparison of Different Systems

References	[42]	[81]	[82]	[86]	[87]	**Work Done**
Application	PIVC	PIVC	CVC	PIVC	Biopsy	CVC
Technologies	BIOZ	US, NIR, FS	US, BIOZ, FS, Vision	US, EM, FS	OCT, Haptic	US, BIOZ, Haptic
Needle Electrodes	2	N/A	2	N/A	N/A	4
Ave. Operation Time (s)	16.9	N.R.	N.R.	90 ± 30	N.R.	22.0
Robotic Automation	Semi-Autonomous	Autonomous	Autonomous	Handheld	Assistive	Assistive
Vein Entry Failure Rate	$14 \pm 4.9\%$	0%	0%	13%	N/A	0%
σ (mm)	N.R.	N.R.	0.52	N.R.	N.R.	0.35
RMSE (mm)	N.R.	N.R.	1.71	N.R.	N.R.	0.66
Mean Error (mm)	N.R.	0.22 ± 0.05	N.R.	0.23 ± 0.17	5.45 ± 3.31	0.56

N/A: Not Applicable; N.R.: Not Reported

3. A NOVEL HAPTIC-ASSISTED BIOZ NEEDLE SYSTEM

CVC is one application that needs precise needle guidance. Although its failure rate is now very low, in regions with scarce medical resources, a precision-guided system is far more valuable than a costly, experienced physician. Therefore, developing a CVC-specific needle insertion system remains of great research value.

This chapter presents a haptic-enhanced bioimpedance needle designed for precision navigation in CVC with millimetre-level accuracy. Specifically, this system integrates BIOZ sensing with a haptic feedback mechanism to assist clinicians during the catheterisation procedure. Four types of embedded needle probes were developed for high-sensitivity BIOZ measurement. These probes are integrated with a compact electronic handle system that enables real-time BIOZ data acquisition and wireless communication, allowing for immediate tissue classification and haptic feedback to optimise needle trajectory guidance. In 24 experimental trials involving user participation with a phantom model, the system demonstrated a 100% success rate in venous entry, achieving a root mean square error (RMSE) of 0.66 mm and an 87% probability of reaching a position within ±1 mm of the vein's centre. The compact and portable design ensures compatibility with clinical environments, laying a solid foundation for future advancements in robotic-assisted CVC and similar procedures.

As discussed in previous literature, many existing electrical measurement techniques exhibit instability and are not well-suited for deep vein access, which is critical for CVC procedures. This limitation primarily stems from two factors. Firstly, most prior research has relied on commercial electromyography (EMG) needles with concentric electrodes at the tip [39], [40], [53]. In BIOZ applications, this bipolar electrode configuration typically introduces electrode polarisation effects, resulting in measurement errors and data instability. In contrast, the four-electrode BIOZ needles

reported in the literature eliminate polarisation effects. However, these designs primarily target biopsy applications, with electrodes mounted along the needle shaft, which is unsuitable for needle navigation and complicates the manufacturing process. Consequently, this chapter focuses on the development of embedded electrodes tailored to meet the specific requirements of CVC.

Secondly, with US assistance, achieving real-time impedance-based centring of the needle in the z-direction remains a challenge. Proper needle entry requires the tip to be precisely advanced to the centre of the vein. Inaccurate depth—whether too shallow or too deep—complicates the subsequent guidewire insertion, which is a critical step for successful catheter placement during CVC. Achieving consistent centring solely based on BIOZ data is challenging, prompting the exploration of multimodal approaches. A dual collaborative robotic arm system integrating US imaging and bipolar BIOZ sensing for autonomous venous access was reported in the literature, achieving a positioning RMSE of less than 1.7 mm under laboratory conditions [82]. However, the clinical translation of this approach is hindered not only by its high cost and bulky equipment but also by the complexity of regulatory approval and the requirement to establish a robust Quality Management System (QMS). Beyond compliance with IEC 60601 standards for electrical safety, medical devices must implement and maintain a QMS in line with ISO 13485 (and FDA QSR 21 CFR 820 in the U.S.) and satisfy comprehensive regulatory frameworks, such as EU MDR 2017/745 and U.S. FDA requirements, before they can achieve clinical certification.

This chapter would introduce a unique combination of BIOZ and haptic feedback through an integrated platform, as shown in Fig. 3.1. The needle employs removable probes inserted in the needle for BIOZ measurements, which drive a haptic engine to provide tactile cues for centring the vein along the vertical axis. Unlike the bulky setup of previous systems, this platform is compact and portable, integrating all electronics into a wireless BIOZ needle handle (BiNH). The handle is attached to Inverse 3, a haptic device by Haply Robotics (Montreal, Canada), providing an intuitive and remote solution for better needle navigation in CVC.

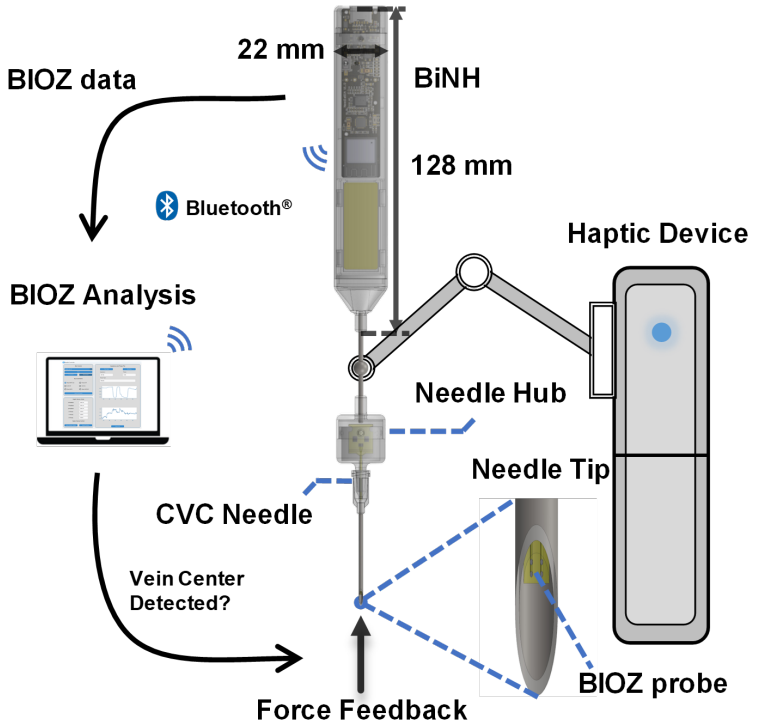

Fig. 3.1. The integrated BIOZ and haptic-driven needle platform for safe and accurate placement of a central venous catheter (CVC) needle.

3.1 Embedded BIOZ Probe Design

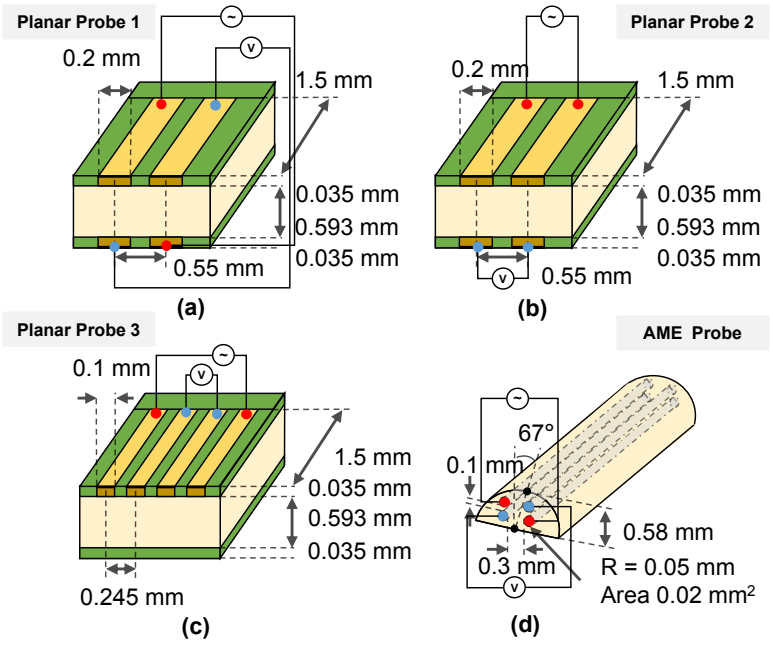

Fig. 3.2. (a) to (c) show the dimension and the electric connection ways for the planar probe, which is made from the PCB. (d) also show the same parameters for the AME probe.

Before designing the embedded BIOZ probe, it was necessary to select an appropriate needle type.

In this study, a 16-gauge needle was chosen, featuring an outer diameter of 1.651 mm and an inner diameter of 1.194 mm. Based on these dimensions, several compatible probe designs were developed. All designs were tailored according to current PCB manufacturing processes and the requirements of additively manufactured electronic circuits (AME) technology provided by Nano Dimension (Massachusetts, United States). The design details are illustrated in Fig. 3.2, which presents the specifications of each device.

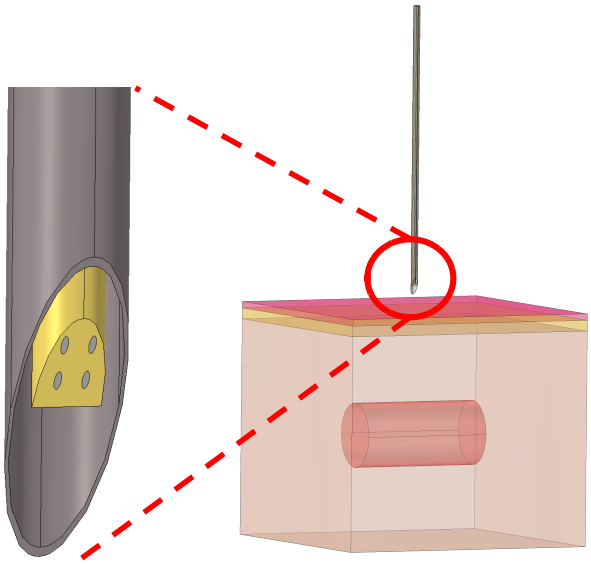

Fig. 3.3. The FEM 3D model in the COMSOL software.

With the reference needle model established, we can now analyse its sensitivity distribution, DOI, and its capability to distinguish conductivity variations across different tissue layers. In this section, the characteristics of the AME probe are investigated through COMSOL simulations. Other probes exhibit similar performance, with differences primarily in the measured impedance values. For instance, the planar probe generally demonstrates lower impedance readings. The primary reason for this difference lies in the electrode size. Specifically, smaller electrodes result in a higher density of electric field lines near the electrode surface. As a result, the potential difference between two measurement points increases due to the intensified electric field gradient, leading to higher measured impedance values. The finite element method (FEM) 3D model in COMSOL is shown in Fig. 3.3.

Table. 3.1. Electrical conductivity and relative permittivity of different tissues and probe materials

Tissue Type	Electric Conductivity (S/m)	Relative Permittivity (1)
Fat	0.024414	92.885
Skin (dry)	4.5128e-4	1119.2
Skin (wet)	0.065836	15357
Fat	0.024414	92.885
Muscle	0.36185	8089.2
Muscle complex	0.315, 0.105, 0.105	1.31e6, 5.2e5, 5.2e5
Blood	0.7029	5120
Acrylic	1e-18	2.1
Silver	2.21e7	1
Steel	1.74e6	1

The conductivity values used in the aforementioned model are referenced from [92]. The specific values are listed in Table 3.1. Based on this model, several aspects need to be explored. Firstly, it is important to determine whether the needle can distinguish impedance differences and the probe sensitivity when placed in tissues with varying conductivities. As shown in the simulation, when the needle is inserted into muscle tissue, the measured impedance is approximately 315.45 Ω. In contrast, in the vein region, which has a higher conductivity, the impedance reduces to 167.82 Ω. Fig. 3.4 presents the sensitivity heatmap (unit is dB) of the needle in the xz cut plane. The red regions indicate high sensitivity, while the blue regions represent low sensitivity.

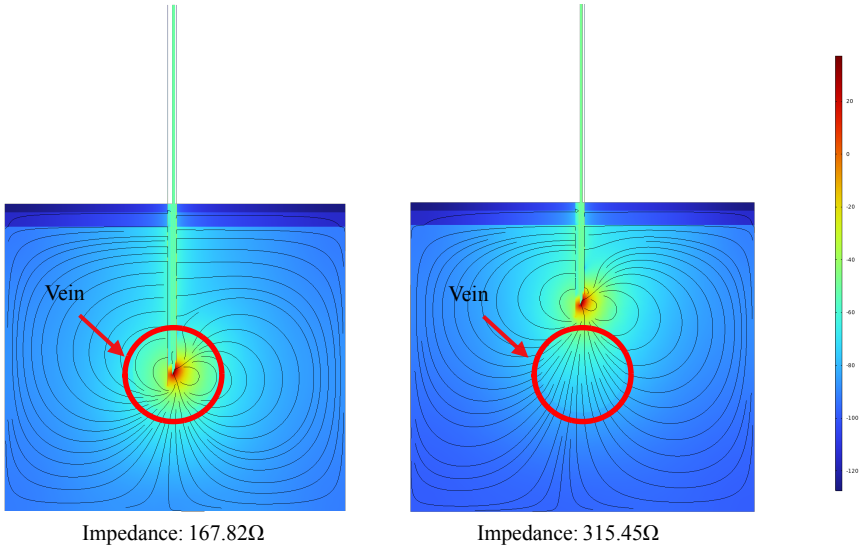

Fig. 3.4. The heatmap of the sensitivity of the BIOZ probe in vein (left) and in muscle (right).

The figure illustrates that the primary sensitivity region is concentrated around the surface of the

probe electrodes. However, the image on the right clearly shows that the sensitivity to conductivity changes is significantly higher in the vein region compared to the surrounding muscle tissue. This is attributed to the higher conductivity of blood veins, resulting in a greater current density within the vein compared to the muscle at the same distance. Due to the finite resolution of the FEM mesh, resolving stable impedance values for micron-scale depth variations near the vein entry point is challenging. This limitation arises because minor insertion depth changes may fall within the same mesh element, leading to considerable measurement noise. To address this, we adopted an alternative approach by interpreting the insertion depth variation as a change in the conductivity distribution within the probe's field of view. Specifically, as the needle approaches the vein wall without penetrating it, the observed conductivity beneath the probe gradually increases. Therefore, Fig. 3.5 illustrates the impedance variation as the vascular conductivity is swept to simulate the effect of incremental depth changes.

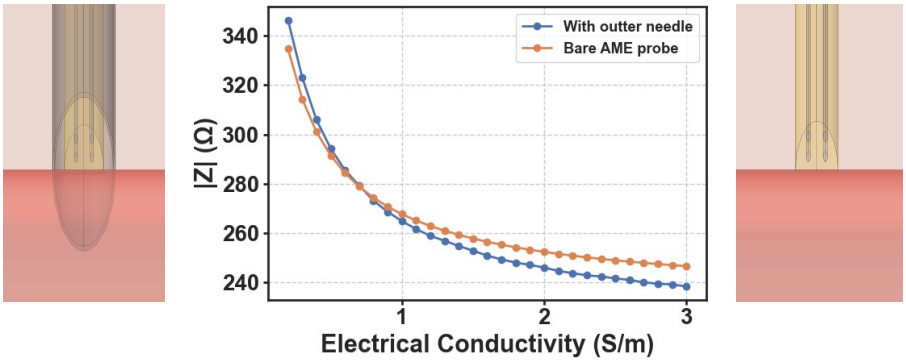

Fig. 3.5. Impedance variation with electrical conductivity for bare AME probe and outer needle configurations.

In the simulation, the needle is positioned directly above the vein wall, almost in contact, to better validate how changes in underlying conductivity affect the measured impedance. To eliminate the influence of the conductive steel outer needle, a bare AME probe configuration was employed for verification. The results indicate that under this probe setup, variations in the conductivity beneath the needle produce significant changes in impedance. This suggests that during needle insertion, it is possible to detect the proximity of the vein based on impedance changes. As previously mentioned,

if the needle is moved further away from the vein and the experiment is repeated, the impedance variation becomes less pronounced. In practical terms, this implies that the farther the insertion point is from the vein, the smaller the impedance change will be during insertion. Therefore, a highly sensitive and low-noise impedance measurement system is crucial to reliably detect these subtle changes. The word done, however, lacks the capability for proximity-based measurement, highlighting a critical research gap for the next phase of development.

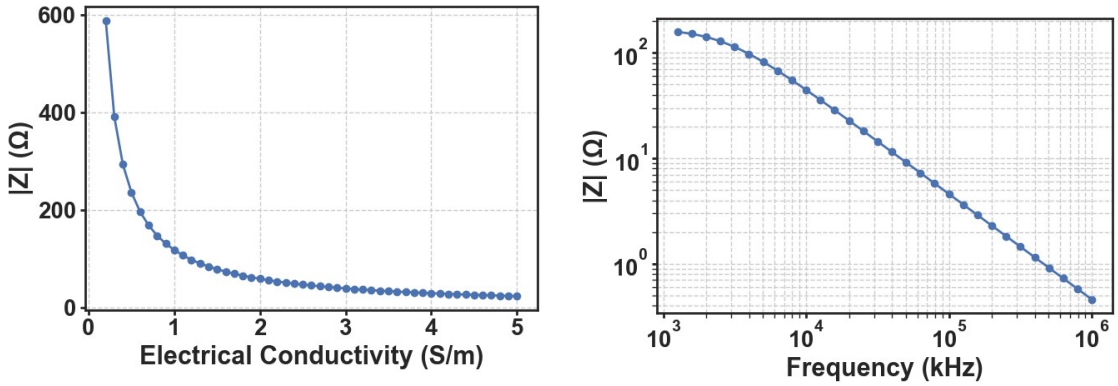

Fig. 3.6. Impedance variation with electrical conductivity (left) and impedance variation with frequency (right).

Additionally, some basic sweep simulations in COMSOL are essential. Fig. 3.6 illustrates the impedance variation as a function of electrical conductivity and frequency sweeps, showing a trend that aligns with theoretical predictions. After the BIOZ probe was fabricated, its real impedance readout was analysed. Electrochemical Impedance Spectroscopy (EIS) measurements were performed over a frequency range of 1 kHz to 1 MHz using an MFIA impedance analyser (Zurich Instruments, Switzerland). Saline solutions with varying conductivities were prepared by dissolving 1.5 g, 2.5 g, 4.5 g, and 6.5 g of salt in 500 ml of deionised water. This resulted in conductivities of 0.56 S/m, 0.90 S/m, 1.54 S/m, and 2.18 S/m, respectively, as measured by an HI 8733 conductivity meter (Hanna Instruments, United Kingdom), as shown in Fig. 3.7.

Although all designs could differentiate between various saline concentrations, the closely matched impedance readouts in the planar probes may hinder subject identification in high-noise environments. In contrast, the AME probe demonstrates improved SNR across the frequency

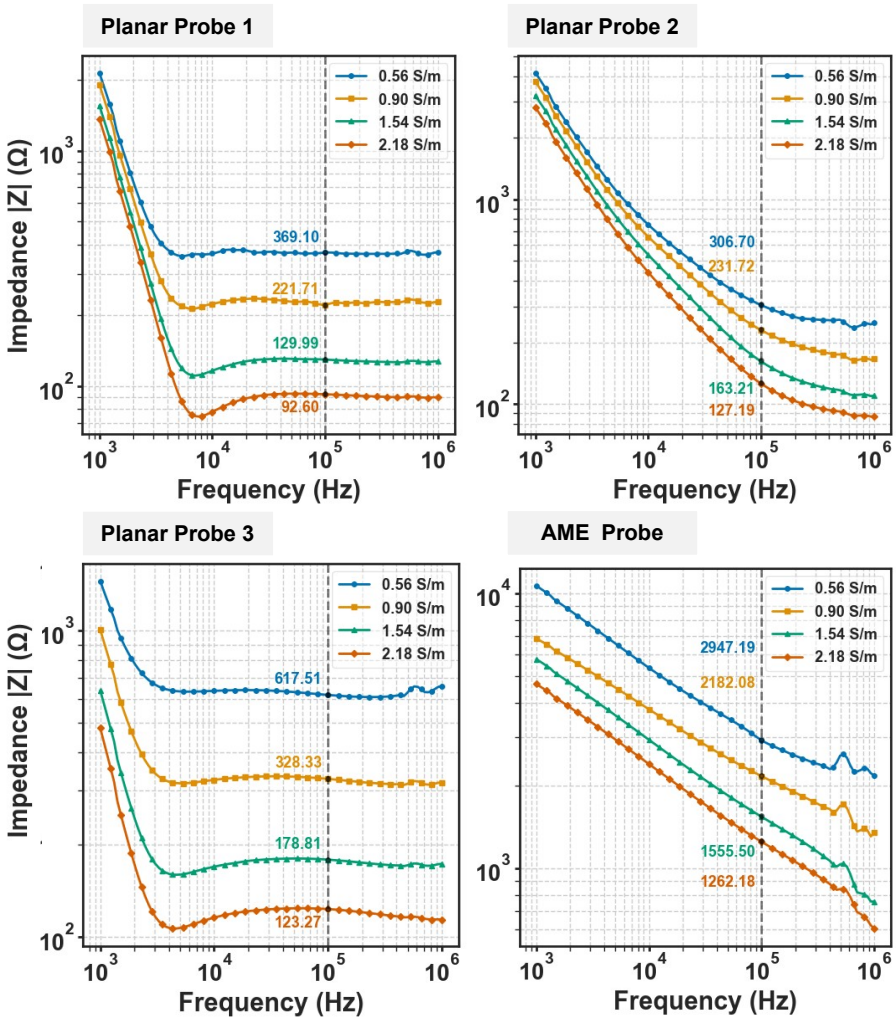

Fig. 3.7. Electrochemical impedance spectroscopy (EIS) measurements of the four probes in four different saline concentrations. The figure annotates the reference impedance values for an injection current at 100 kHz.

spectrum. This observation aligns well with the previously FEM-analysed EIS curves, although the measured impedance values are significantly higher. This discrepancy is likely attributed to parasitic capacitance between connectors and the introduction of wire impedance during practical measurements, which can notably affect the readout accuracy. The following section would be based on this BIOZ probe to build the system.

3.2 System Design

Fig. 3.8 illustrates the complete system structure, which comprises a BiNH, a host laptop, and a haptic device. The BiNH records impedance data from the BIOZ probe while registering the handle's

orientation via the inertial measurement unit (IMU) and transmits the information via Bluetooth low energy (BLE) 5.0 to the host PC. The host PC also records data from the haptic device, together with the BiNH data, to determine the needle insertion distance. Additionally, the host PC synchronises all data for tissue classification and calculates the end force of the haptic device and provides feedback to the user to indicate that the vein's central region is reached.

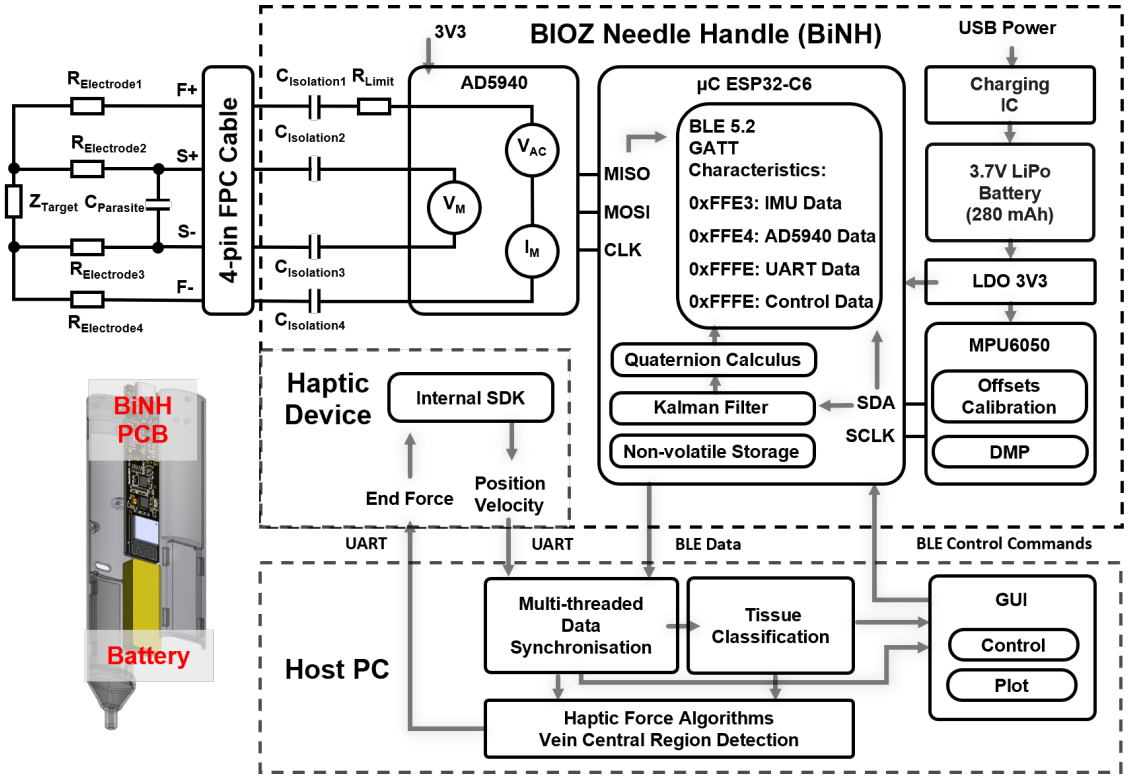

Fig. 3.8. System architecture of the BiNH with the host computer and haptic device.

As illustrated in Fig. 3.8, the BiNH system employs a high-precision impedance readout front end, the AD5940 (Analogue Devices, Massachusetts, United States), for BIOZ measurements using a tetrapolar configuration. This setup allows the system to sample at 800 kbps and perform internal impedance demodulation via discrete Fourier transform (DFT). The AD5940 outputs impedance data directly in real and imaginary components through SPI communication, providing high-resolution impedance readings. In this study, a 400 $\mathrm{mV_{pk\text{-}pk}}$ sinusoidal signal at 100 kHz was applied, with the DFT operating on 4096 points, resulting in an impedance output frequency of 100 Hz. The tetrapolar connection points from the BiNH, labelled as $\pm F$ and $\pm S$, were linked to the BIOZ probe inside the needle hub via a flexible PCB (FPC) cable (see Fig. 3.1), forming a complete BIOZ needle.

The choice of 100 kHz as the operating frequency and 4096 as the number of sampling points was deliberate. Since the ADC sampling rate of the AD5940 is 800 kbps, this configuration allows the 100 kHz signal to be evenly divided, yielding exactly 512 samples per cycle. This precise division ensures the sampling window is perfectly aligned with the signal period, eliminating phase discontinuities and minimising measurement errors. Additionally, 100 kHz falls within the optimal frequency range for distinguishing tissue types, as reviewed in Chapter 2, making it particularly suitable for impedance-based tissue differentiation.

The BiNH circuit is further integrated with an ESP32-C6 (Espressif, China) and an IMU MPU6050 (InvenSense, TDK, United States), which incorporates a digital motion processor (DMP) with an embedded Kalman filter. This configuration provides stable and accurate handle orientation estimation, with drift limited to less than 1 degree after 20 minutes of continuous movement. To optimise power consumption while maintaining performance, the BLE notification characteristic is configured at 30 Hz. At full operational speed, the total power consumption of the system is 203.5 mW, with 178 mW attributed to the BLE module, supporting up to 5 hours of continuous operation. In light sleep mode, power consumption is reduced to 4.5 mW, extending standby time to over ten days.

The host PC manages two primary functions:

- **Tissue Classification**: A thresholding algorithm is used to classify the detected impedance values into three distinct tissue types: air, muscle, and blood. This real-time categorisation facilitates better trajectory planning during needle insertion.

- **Haptic Force Feedback**: As depicted in Fig. 3.8, the multi-threaded data streams from the BiNH are synchronised and processed by the force feedback algorithm. The total force applied during needle insertion is calculated as follows:

$$\begin{aligned}\overrightarrow{F_{\text{total}}} &= m \cdot \overrightarrow{F_{\text{drag}}} + n \cdot \overrightarrow{F_{\text{catch}}} \\ \overrightarrow{F_{\text{catch}}} &= k_s \cdot \left(\overrightarrow{P_{\text{nearest}}} - \overrightarrow{P_{\text{device}}}\right) \\ \overrightarrow{F_{\text{drag}}} &= k_d \cdot \overrightarrow{V_{\text{device}}}\end{aligned} \tag{3.2.1}$$

Here, $\overrightarrow{F_{\text{drag}}}$ and $\overrightarrow{F_{\text{catch}}}$ represent the force components simulating tactile sensations during tissue penetration. The coefficients m and n are adjusted according to the detected tissue type to modulate force perception. The parameters k_s and k_d are the capture stiffness and drag coefficients, respectively, and are fine-tuned based on practical scenarios to enhance realism during insertion. Furthermore, P_{nearest} denotes the nearest capture grid point, dynamically computed based on a finely meshed virtual grid structure. This grid-based positioning not only ensures smooth trajectory adjustments but also mitigates erratic force feedback caused by sudden velocity changes or gravitational effects. The term P_{device} refers to the current position of the needle, while V_{device} is its instantaneous velocity. The real-time force feedback mechanism is tightly coupled with both the impedance data and the needle's pose, position, and velocity. This synchronisation allows the operator to sense subtle tissue transitions during insertion, enhancing both precision and safety. As a result, the system not only improves trajectory accuracy but also provides an intuitive tactile experience for clinicians, bridging the gap between robotic assistance and manual dexterity.

3.3 Experiment Setup

Based on the complete hardware and software system, two experiments were conducted to evaluate its performance. The first experiment aimed to validate the real-time capability of the system. A robotic arm UR3e (Universal Robots, United States) was used to drive the discrete BiNH needle system into a hydrogel-based phantom. The insertion process was controlled via programmed commands, setting the UR3e insertion speed to 1 mm/s with a total insertion depth of 25 mm. Prior to the experiment, the exact thickness of the phantom was measured, allowing for precise estimation of the

needle's position during insertion and the expected moments of impedance changes. By continuously acquiring and recording impedance data throughout the insertion process, the real-time performance of the system could be effectively assessed. The collected impedance data were then plotted on a single graph, clearly illustrating the moment of transition as the needle penetrated different layers within the phantom. This experimental setup is illustrated in Fig. 3.9.

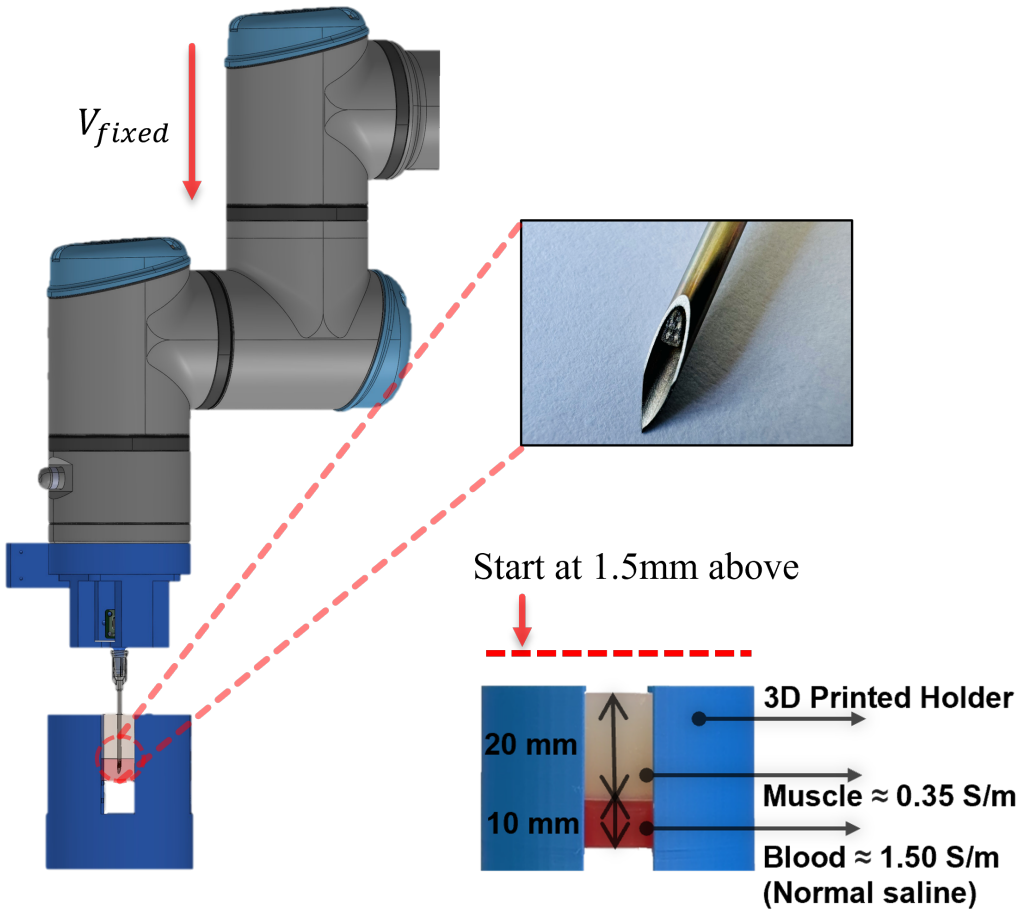

Fig. 3.9. Robotic arm insertion experimental setup.

The testing phantom, as depicted in the figure, consists of two hydrogel layers simulating muscle and blood tissues. The muscle hydrogel was prepared by mixing 15 g of agar, 0.6 g of salt, and 500 ml of water, while the blood hydrogel contained 15 g of agar, 4.5 g of salt, and 500 ml of water. These two layers were stacked vertically to form the test phantom, representing the tissue structure for evaluation. As mentioned earlier, it is assumed that the vascular position along the x-axis is pre-determined using US imaging. The primary objective of this experiment is to utilise the BIOZ sensing

system to precisely locate the vascular centre along the z-axis during insertion. This is the reason why the phantom was designed with a flattened, layered structure.

The second experiment was conducted using the same hydrogel-based phantom as in the first experiment. However, the primary distinction lies in the use of a haptic device combined with a graphical user interface (GUI) to facilitate user-interactive needle insertion, as shown in Fig. 3.10.

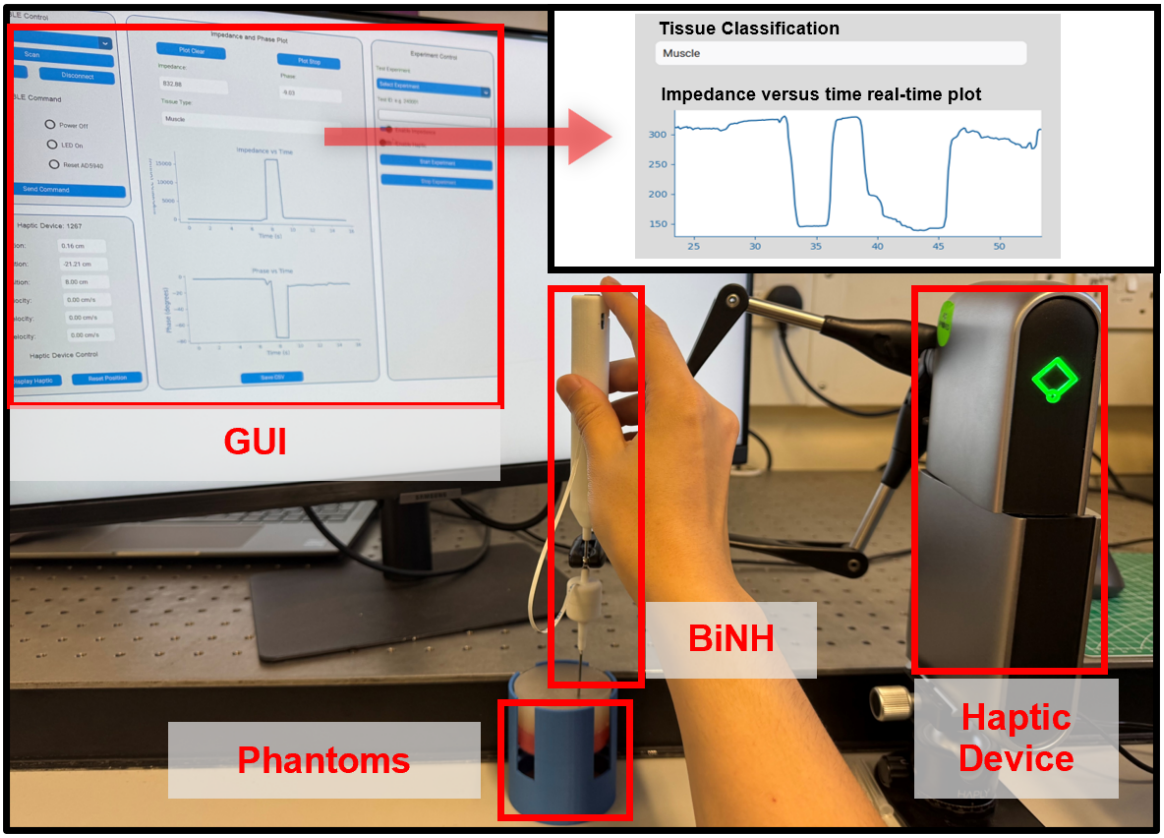

Fig. 3.10. User-controlled experimental setup.

The experiment involved user-controlled needle insertion into the vein centre under three different conditions:

- **Unaided Insertion (case 1)**: In this scenario, participants inserted the needle manually without any visual or haptic assistance. The only sensory feedback came from tactile sensations as the needle punctured the muscle layer and entered the vein. Participants were only informed about the approximate thicknesses of the muscle (2 cm) and the vein (1 cm) layers, mimicking conventional CVC procedures.

- **Impedance-Guided Insertion (case 2)**: In the second case, a real-time graphical user interface

(GUI) displayed the BIOZ data measured from the phantom during insertion. Although no haptic feedback was applied, the impedance changes corresponding to different tissue types (muscle and vein) were visually represented, allowing participants to identify the tissue transition points more easily. The aim was to evaluate the benefit of impedance-based visualisation on the accuracy and speed of CVC.

- **Haptic and Impedance-Guided Insertion (case 3)**: The final case introduced both haptic feedback and real-time impedance visualisation. The haptic device applied varying resistance based on the measured impedance changes. For instance, when the needle approached or entered the vein, a noticeable increase in resistance was applied, mimicking the sensation of penetrating vascular tissue. This real-time force feedback provided a more intuitive experience, allowing participants to adjust insertion force accordingly and avoid overshooting the vein. When the needle tip is close to the centre of the vein, the user would feel a high-resistance wall to prevent further insertion.

Prior to the experiment, participants received brief instructions but were not allowed to practise with the device, ensuring that learning biases were minimised. The order of the three conditions was randomised for each participant to further reduce potential biases. Each condition was repeated 24 times across 8 participants, none of whom had prior experience with CVC procedures. Ethical approval for this study was obtained from the Ethics Committee of University College London (ID: 27647/003). Additionally, the system is designed to accommodate more conventional CVC needles, such as the 18-gauge variant, by scaling the probe size accordingly. This flexibility suggests that the system is adaptable to standard clinical equipment, enhancing its potential for clinical translation.

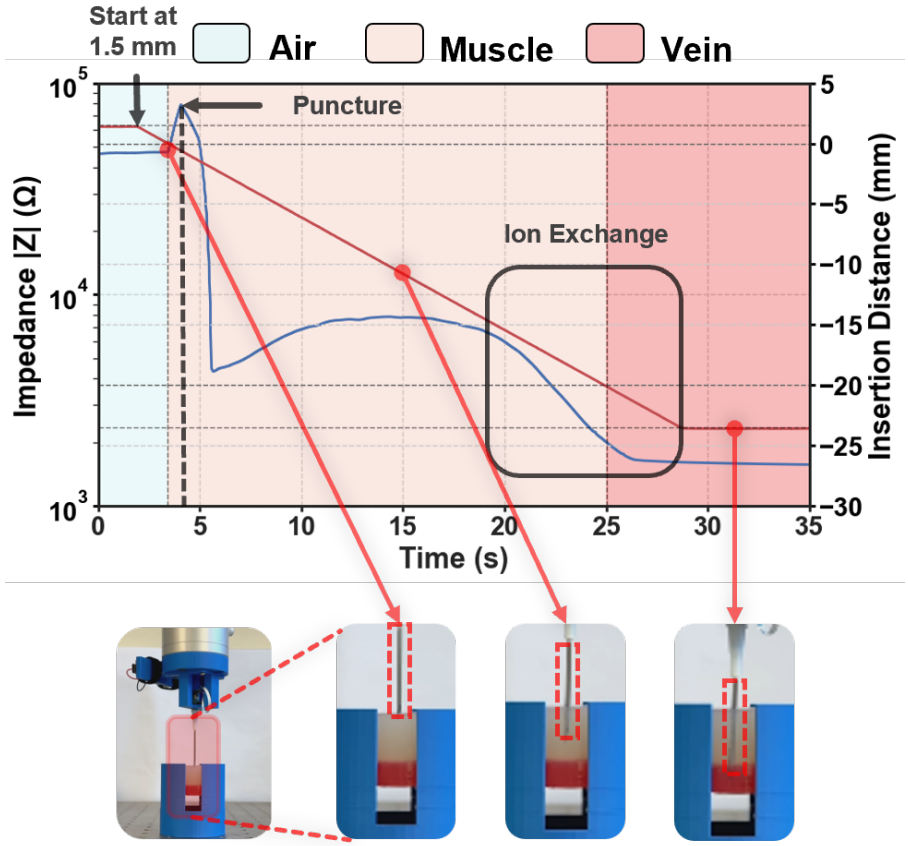

Fig. 3.11. Impedance (blue curve) and insertion distance (red curve) as functions of time during needle insertion. The sequential images show the needle's position at different time points, corresponding to the red markers on the curves.

3.4 Results and Discussion

The results of the first experiment are illustrated in Fig. 3.11, which shows the impedance variation and the robotic arm's insertion distance as a function of time. At an insertion depth of 0 mm, the needle tip is just touching the phantom interface. As the insertion progresses, the impedance increases steadily until puncture occurs, after which it drops abruptly and stabilises once the needle fully crosses the interface. This behaviour is attributed to changes in the contact area and insertion force between the hydrogel and the electrode, as well as ion exchange between the hydrogels, which gradually reduces conductivity near the contact surface. With precise robotic control, the exact point at which the needle enters the blood-mimicking hydrogel is accurately determined. Upon reaching the final insertion position, stable impedance readings were observed. These empirical impedance

parameters were subsequently used to adjust thresholds for reliably distinguishing between different tissue types in further experiments. The impedance update interval is 10 ms. Combined with control communication and processing time, the system achieves an update rate of over 90 fps, ensuring real-time responsiveness. Overall, the impedance variation correlates with the insertion depth, validating the system's real-time performance.

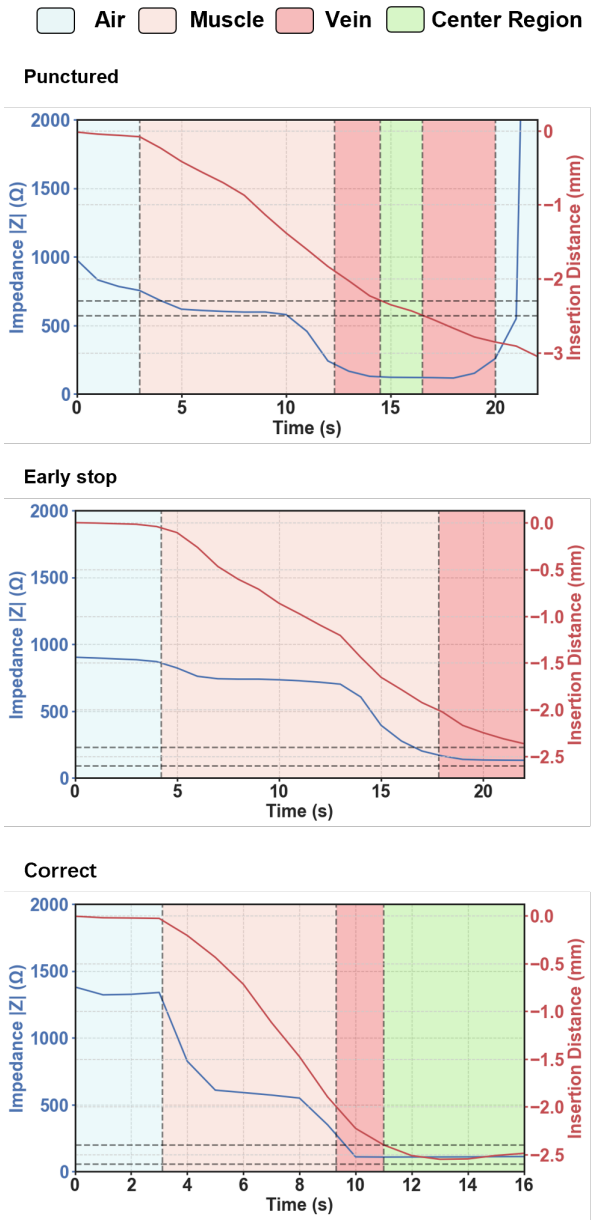

Fig. 3.12. Impedance variation with insertion depth for three characteristic samples

As for the second experiment, multiple outcomes were observed where the needle was misplaced, as illustrated in Fig. 3.12. The first two results show that the needle completely penetrated the vessel and entered the air region. This phenomenon occurred most frequently in Case 1, primarily due to

the operator's lack of awareness regarding the insertion depth, leading to vessel perforation. Another outcome observed was premature stopping, which was most common in Case 2. Although impedance feedback was available, the operator's uncertainty about the exact insertion depth resulted in the needle halting prematurely in the upper region of the vessel. In contrast, Case 3 demonstrated the highest success rate, with the needle consistently positioned at the centre of the vessel.

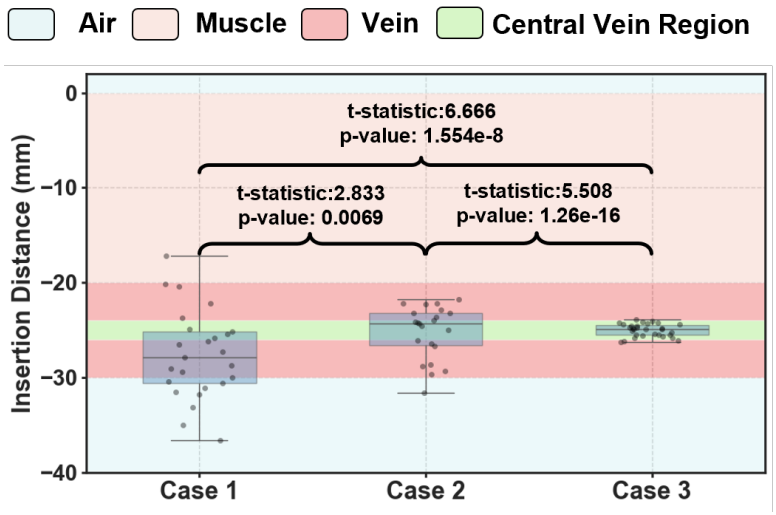

Fig. 3.13. Impedance Variation with Insertion Depth for Three Characteristic Samples

Fig. 3.13 presents a box plot illustrating the final needle tip positions across 24 trials for each experimental case. Statistical analysis using absolute insertion distance error, t-statistics, and p-values clearly indicates that Case 3 achieved the highest insertion accuracy. Specifically, without any assistance, only 68% of the trials successfully accessed the vein. This success rate significantly increased to 95.45% with the aid of tissue classification and further improved to 100% with the addition of haptic feedback. Within the vein region, the centre is defined as being within ±10% of the vein radius (i.e., within ±1 mm of the vein centre), which is highlighted with green bars in the plot. Case 3 again demonstrated the highest centring accuracy, achieving 86.7%, whereas Case 1 and Case 2 achieved only around 16%. For Case 3, the system's navigation accuracy was quantified with a standard deviation (σ) of 0.35 mm, a root mean square error (RMSE) of 0.66 mm, and a mean error (ME) along the vertical axis of 0.56 mm. The complete results for the experiment in three cases are shown in Table 3.2.

Table. 3.2. Vein Entry Rate and Central Vein Region Rate Comparison for Different cases

Metrics	Case 1	Case 2	Case 3
Enter Vein Rate	68%	95.45%	100%
Central Vein Region Rate	16%	16%	86.7%

3.5 Conclusion

This paper introduces an innovative BIOZ-guided haptic needle system specifically designed for CVC procedures. To enhance the performance of the embedded tetrapolar measurement, four distinct probes were developed and validated, including a high-SNR AME probe capable of distinguishing varying conductivity levels. The system, compact and portable, enables real-time BIOZ analysis and needle orientation tracking while seamlessly integrating with a haptic device for CVC applications. Experimental validation on phantom models demonstrated a 100% success rate in venous entry, along with an 87% centring accuracy. Across 24 trials, the system achieved a vertical insertion RMSE of 0.66 mm. These results indicate that the proposed platform has the potential to significantly enhance CVC procedures, enabling faster, more reliable operations that benefit both clinicians and patients.

4. FUTURE WORK

4.1 Hypothesis of Study

This chapter presents the work plan for the remaining phases of the PhD research. As discussed in Chapter 3, the preliminary efforts were limited to prototype validation. Following this, we would identify the principal gaps that persist in this field and formulate clear hypotheses to address them. We then outline proper methodologies that will push the research frontier and close these gaps.

4.1.1 Electrode Design and Algorithms

Hypothesis 1: By arranging electrodes along both the axial and radial directions and by optimising injection strategies and electrical impedance tomography (OEIT) algorithms, we could extend measurement detail and enlarge the sensitivity space along the needle.

OEIT is an extension of EIT, in which electrodes placed on medical tools like needles or catheters are used to reconstruct the surrounding tissue's conductivity distribution outward from the probe [93].

A key challenge in our current research is that the effective sensitivity volume around each electrode on the needle shaft is extremely limited, restricting OEIT reconstructions [93] to only the immediate vicinity of the needle surface. This limitation reduces the meaningfulness of the image reconstructions in comparison with a single-site impedance recording. To address this, we propose the electrode layout shown in Fig. 4.1. Electrodes are distributed axially and radially along the needle. Multiple ring electrodes at different axial positions enable true three-dimensional OEIT measurements. Luo et al. mounted 32 electrodes on a 5 mm catheter and used OEIT to detect lipid-rich plaques in blood vessels [93]. They built a finite-element mesh in EIDORS, discretised the Laplace equation, and solved for conductivity via Gauss–Newton regularisation. Despite this, they

may still not accurately detect small, distant lipid plaques. The root cause was the small sensitivity region of conventional methods and the lack of structural prior information to enhance imaging. Shen et al. tackled the problem of defining a finite domain for OEIT's infinite external region. They mapped the external space to a unit polar circle, ensuring that all measurements contribute to the reconstruction. They also used B-spline boundary priors for rapid contour estimation. By restricting Landweber iterations to the region of interest (ROI), they reduced computational load, though at the cost of more iterations [94]. This approach boosted OEIT efficiency but still suffered from limited sensitivity and required manual tuning of the ROI threshold without feedback. Zamani et al. improved precision by automatically generating an airway-tree skeleton as a prior [95]. They computed impedance only within that skeleton, effectively suppressing background noise.

Inspired by these advances, we propose to fuse ultrasound-derived boundary priors with our multi-electrode needle. The ultrasound map will inform a refined ROI that closely follows the surrounding tissue interface. Coupled with the new axial and radial electrode rings, this strategy should enlarge the OEIT sensitivity volume and permit deeper impedance sampling along the needle tip. Finally, we will integrate multi-frequency measurements [39] to perform differential imaging and capture additional structural details. Additionally, related circuit systems should also be developed to fit the real-time and high-speed bioimpedance demodulation and conductivity matrix reconstruction.

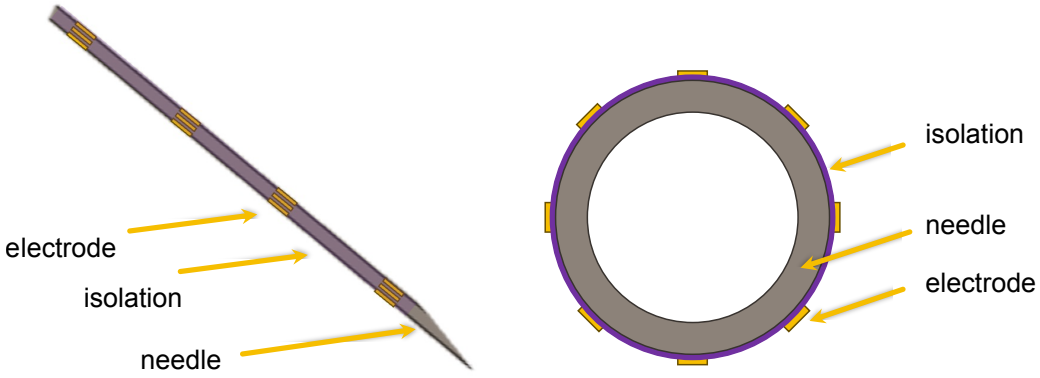

Fig. 4.1. A suggested new electrode design.

4.1.2 Ultrasound Reconstruction Algorithms

Hypothesis 2: By employing IMU and visual calibration drift errors, empowered by diffusion AI models and other image processing neural network models, the work aims to advance current 3D model construction of human tissue using ultrasound.

Many studies focus on single structures, such as bone, blood vessels, or common organs volumetric reconstruction [14], [96]–[98]. A few works have addressed nerve modelling [99], [100], and U-Net and its variant M-Net can now segment target nerves in isolation [101]. However, comprehensive structural segmentation and modelling of multiple tissue types remain unexplored gaps. Specifically, freehand scanning introduces poorly compensated positioning errors, while real-time segmentation and reconstruction of various tissues can impede the system's real-time performance. To address these challenges, our system integrates IMU and visual tracking for motion compensation, alongside self-supervised learning and deep implicit networks [102], [103]. We would also employ continuous-frame convolutional neural networks to guide real-time diffusion updates and accelerate reconstruction. Ultimately, this approach enables freehand ultrasound to achieve online or near-real-time 3D structural reconstruction. With the aid of a detailed 3D reconstructed tissue model, we can design accurate needle path strategies, including insertion angles, minimally invasive trajectories, and necessary detours around nerves.

4.1.3 3D Haptic Guidance Algorithms

Hypothesis 3: By incorporating a mechanical model of the needle, enforcing a centreline algorithm during insertion, and applying reinforcement learning (RL) for path and force–feedback adjustment, together with realistic tissue force simulation, we can achieve more accurate needle guidance.

Zamani et al. applied a 2.5D multi-view centreline navigation technique to cochlear electrode insertion. They computed the distance from the electrode tip to both the inner and outer walls of the scala tympani, the probability of forward-wall collision, and the insertion orientation angle. This

method enabled accurate centreline following and significantly reduced the risk of soft tissue injury [104]. However, it only tracked the leading electrode tip, neglecting the rotation and deformation of subsequent contacts. These unmodelled effects can introduce unpredictable electrode positioning errors. Abbasi-Hashemi et al. used online learning to map the catheter's spatial location to a synthetic force vector, which was then converted into actuator commands via a Jacobian matrix [105]. However, the system's real-time performance and transferability across different settings remain insufficiently validated. To address these limitations, we propose using reinforcement learning to adapt the needle trajectory and haptic force feedback in response to dynamic bioimpedance and ultrasound data. This will be integrated with an optimised centreline navigation algorithm to continuously guide the needle tip along the optimal 3D trajectory. Additionally, we will model the needle's mechanical properties to compensate for tip-induced displacement errors.

Reinforcement learning can adapt the needle trajectory and haptic force feedback in response to dynamic bioimpedance and ultrasound data [105], but its performance depends critically on update rate. To address these limitations, we will model the motion and deformation of multi-electrode segments. We will synthesise their behaviour using the needle's mechanical properties to counteract tip-induced displacement errors. We also integrate RL with an optimised centreline navigation algorithm. This combined approach continuously guides the needle tip along the optimal 3D trajectory.

Current haptic studies often remain confined to 2D tactile feedback or simple elastic constraints along the z-axis [87]. Few studies simulate and amplify reaction forces in layered tissues. To overcome this, we would implement full 3D haptics, allowing the needle tip to move within a virtual tube. We introduced three force components in Chapter 3. Based on those, we proposed piercing force captures the abrupt resistance

$$\vec{F}_{\text{pierce}} = \begin{cases} k_s \left(R - \left\| \vec{P}_{\text{tip}} - \vec{P}_{\text{vessel}} \right\| \right) \frac{\vec{P}_{\text{tip}} - \vec{P}_{\text{vessel}}}{\left\| \vec{P}_{\text{tip}} - \vec{P}_{\text{vessel}} \right\|}, & \left\| \vec{P}_{\text{tip}} - \vec{P}_{\text{vessel}} \right\| < R \\ \overrightarrow{0}, & \left\| \vec{P}_{\text{tip}} - \vec{P}_{\text{vessel}} \right\| \geq R \end{cases} \tag{4.1.1}$$

where k_s is the stiffness, R is the vessel radius, $\vec{P}_{tip}$ is the needle-tip position updated at 200 Hz, and $\vec{P}_{vessel}$ is the real-world vessel position. Meanwhile, insertion friction captures the viscous resistance encountered as the needle advances through tissue. Its magnitude varies with tip speed and is given by:

$$\vec{F}_{\text{insert}} = \begin{cases} -k_d \vec{v}_{\text{tip}}, & \delta < 0 \\ \overrightarrow{0}, & \delta \geq 0 \end{cases} \tag{4.1.2}$$

where k_d denotes the damping coefficient, $\vec{v}_{tip}$ the instantaneous tip velocity and δ is a penetration indicator, meaning if it is in a specific tissue. Together, these two force components reproduce both the sudden resistance of tissue puncture and the continuous drag during insertion.

$$\mathbf{F}_{\text{path}} = nk_s \xi \hat{\mathbf{u}} + mk_d \vec{v}_{\text{tip}} \hat{\mathbf{u}} \tag{4.1.3}$$

whereξ is the unit radial displacement, and m, n are the weighting factors tuned to optimise haptic fidelity.

Finally, these force components are integrated to drive a real-time haptic interface that continuously computes an optimal 3D insertion trajectory and tissue reaction. As the needle approaches sensitive anatomy, the system renders gentle corrective forces to guide it back toward the planned path (see Fig. 4.2). By blending rapid, precomputed tissue responses with on-the-fly trajectory adjustments, our method would provide smooth, clinically realistic tactile cues and help operators maintain safe insertion angles throughout the procedure.

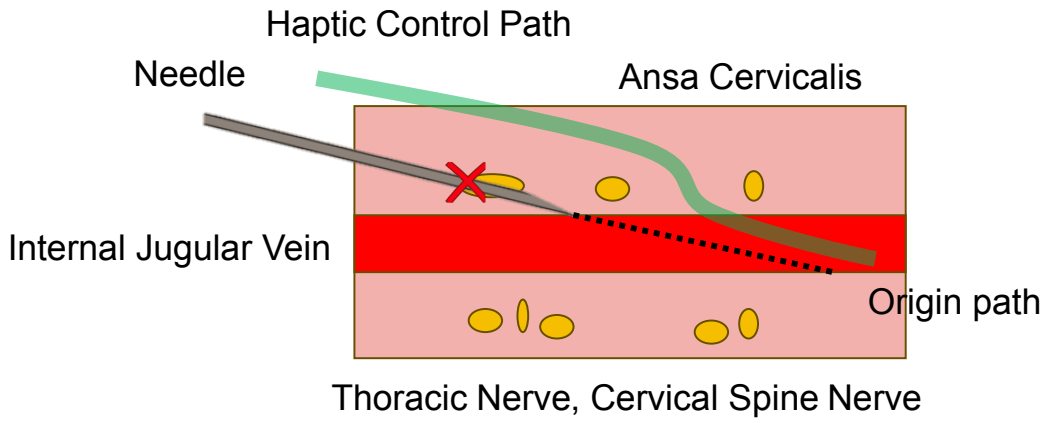

Fig. 4.2. 3D needle trajectory within a haptic constrict tube (green).

4.2 Next Step

Based on the hypothesis outlined above, the next immediate step will be to build the core system and algorithmic framework of the envisioned system. Starting with the realisation of proof-of-concept functionality, then develop and refine more advanced algorithms mentioned in this chapter, addressing each hypothesis in depth. The basic system is shown in Fig. 4.3.

In this system, optical tracking is used to determine the relative position between the ultrasound probe and the needle. Additionally, a single ultrasound B-mode scan provides vessel and tissue size information through spatial rotation and scaling, allowing the target insertion point to be marked directly on the image.

In theory, with a fixed needle insertion angle, this information enables accurate targeting of the desired location. However, due to anatomical variability and non-uniform sub-surface tissue thickness, additional sensing is required. Bioimpedance data are employed to detect the precise moment of vessel entry, triggering a high-priority update of the 3D haptic force.

The haptic interface enforces a virtual constraint, guiding the user to insert the needle at a precise coordinate that yields a trajectory closely aligned with the target. This insertion point can later be recalculated based on more advanced 3D path planning strategies.

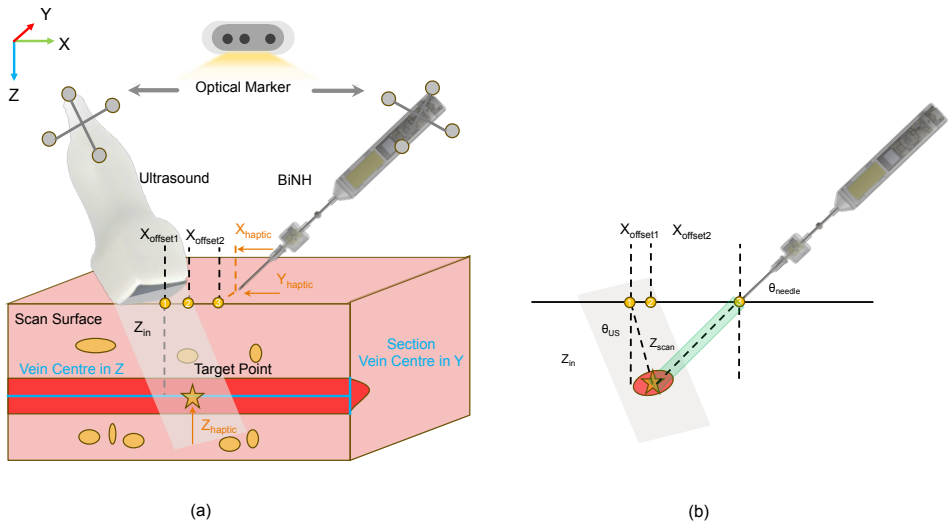

Fig. 4.3. Structure of the proposed system. (a) The blue dashed lines indicate the target insertion centre of the vein along the z- and y-axes. Orange variables and arrows represent haptic corrections that constrain the needle to the correct insertion point and depth, compensating for initial needle positional deviations. (b) illustrates constraints along the x-axis. The green region denotes haptic force limiting the insertion path; this path may induce needle deflection, leading to x-axis inaccuracies. Real-time curvature calibration of the green insertion path is therefore required to correct these errors.

4.3 Challenges in Next Step

Current foreseeable challenges can be categorised into two main aspects. The first concerns the system's need to process large volumes of data, including high-speed BLE bioimpedance signals, IMU measurements, and image data such as optical marker images and ultrasound scan frames, along with the associated post-processing algorithms. While simultaneously executing control algorithms, precise synchronisation of these multi-modal data streams is essential to maintain sub-millimetre accuracy. Furthermore, the parallel execution of multi-sensor processing pipelines introduces significant latency constraints. Addressing these issues requires engineering solutions that incorporate accelerated processing strategies, multi-threaded architectures, and synchronised data structures to ensure system efficiency and stability.

The second major challenge lies in the manufacturing process and packaging of the probe. Given that the needle diameter is in the millimetre range and the embedded BIOZ probe dimensions reach as small as 50 µm, mechanical strength becomes a critical issue. As previously discussed, the AME-

based probe demonstrated limited mechanical robustness. Therefore, it is crucial to explore more durable manufacturing techniques for optimised needle design. One potential solution is to transition the embedded design to a deposition-based approach, where insulating layers and conductive metals are layered directly onto the needle shaft. This strategy may require collaboration with external partners to acquire more reliable needle systems. Additionally, moulding techniques assisted by 3D printing can be investigated to enhance structural design. Finally, partnering with well-established microfabrication and integrated circuit packaging companies may facilitate the realisation of high-strength probes based on the proposed design.

4.4 Publications

The author intends to publish a minimum of two journal articles, along with multiple conference papers, to systematically present the research findings at each stage of the PhD study.

4.5 Gantt Chart

To provide a clearer overview of the PhD project timeline, a Gantt chart is shown below. This chart presents the four-year research process and highlights key milestones. Although the final months allocated for thesis writing and revisions are not depicted, they follow the main research activities. In the chart, dark grey segments denote primary tasks currently in focus, while light grey segments represent secondary tasks that generally run in parallel during this period.

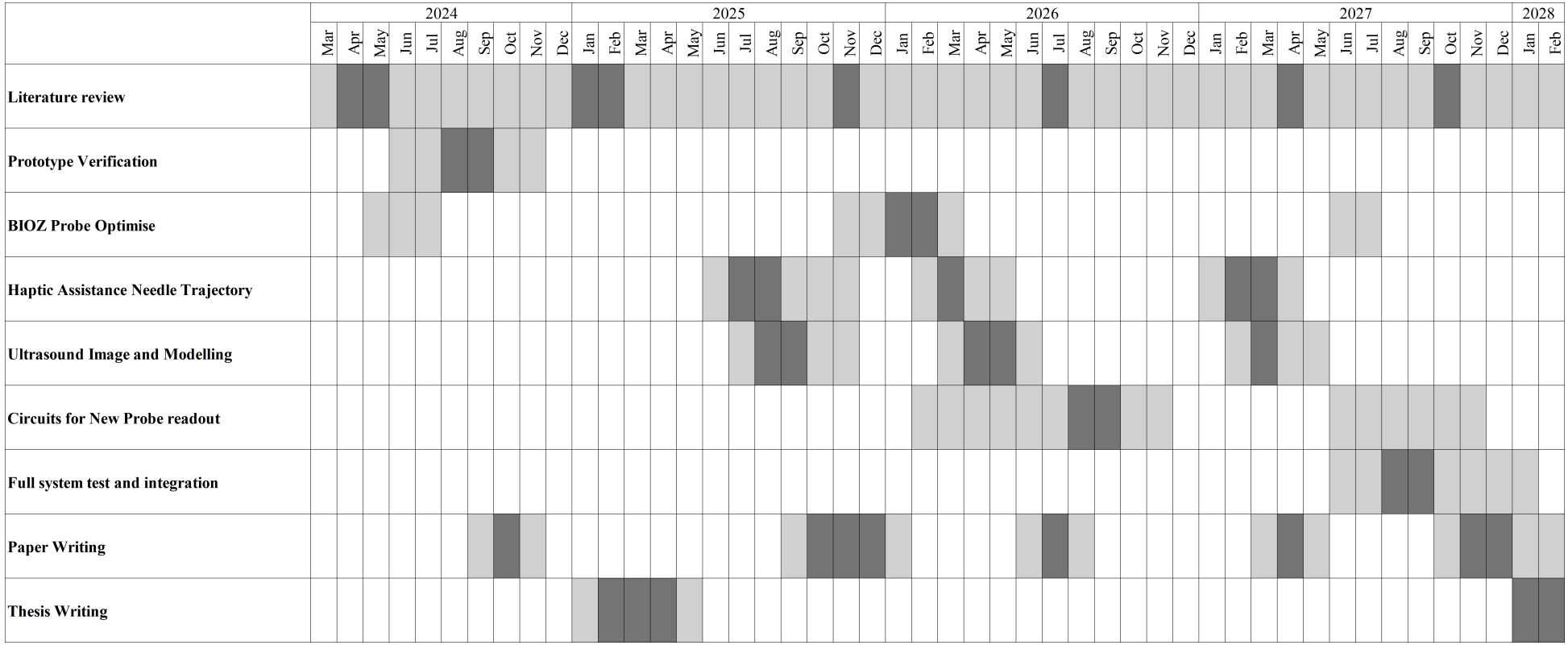
2024
2025
2026
2027
2028
Mar Apr May Jun Jul Aug Sep Oct Nov Dec Jan Feb Mar Apr May Jun Jul Aug Sep Oct Nov Dec Jan Feb Mar Apr May Jun Jul Aug Sep Oct Nov Dec Jan Feb Mar Apr May Jun Jul Aug Sep Oct Nov Dec Jan Feb
Literature review
Prototype Verification
BIOZ Probe Optimise
Haptic Assistance Needle Trajectory
Ultrasound Image and Modelling
Circuits for New Probe readout
Full system test and integration
Paper Writing
Thesis Writing

REFERENCES

[1] J. Park, B. Seo, Y. Jeong, and I. Park, "A review of recent advancements in sensor-integrated medical tools," *Advanced Science*, vol. 11, no. 20, p. 2 307 427, 2024.

[2] *Injection safety: Questions and answers*, 2025. [Online]. Available: `https://cdn.who.int/media/docs/default-source/integrated-health-services-(ihs)/injection-safety/is_questions-answers.pdf?sfvrsn=3f282f31_5`.

[3] Z. Cheng, M. Koskinopoulou, S. Bano, D. Stoyanov, T. R. Savarimuthu, and L. S. Mattos, "Sensing technologies for guidance during needle-based interventions," *IEEE Transactions on Instrumentation and Measurement*, 2024.

[4] M. Lennon, N. Zaw, D. Pöpping, and M. Wenk, "Procedural complications of central venous catheter insertion," *Minerva Anestesiol*, vol. 78, no. 11, pp. 1234–40, 2012.

[5] R. N. Smith and J. P. Nolan, "Central venous catheters," *Bmj*, vol. 347, 2013.

[6] B. Teja, N. A. Bosch, C. Diep, *et al.*, "Complication rates of central venous catheters: A systematic review and meta-analysis," *JAMA Internal Medicine*, vol. 184, no. 5, pp. 474–482, 2024.

[7] B. Saugel, T. W. Scheeren, and J.-L. Teboul, "Ultrasound-guided central venous catheter placement: A structured review and recommendations for clinical practice," *Critical Care*, vol. 21, no. 1, p. 225, 2017.

[8] J. Ye, W. Peng, D. Chen, *et al.*, "Ultrasound-guided percutaneous biopsy of peripheral pulmonary lesions with 16-g core needles: Study of factors that influence sample adequacy and safety," *Clinical Radiology*, vol. 78, no. 1, pp. 24–32, 2023.

[9] J. Kim, C. G. Chee, J. Cho, Y. Kim, and M. A. Yoon, "Diagnostic accuracy and complication rate of image-guided percutaneous transthoracic needle lung biopsy for subsolid pulmonary nodules: A systematic review and meta-analysis," *The British Journal of Radiology*, vol. 94, no. 1127, p. 20 210 065, 2021.

[10] S.-X. Yang, M.-L. Chen, L. Xie, *et al.*, "Procedure-related pain during ct-guided percutaneous transthoracic needle biopsies of lung lesions: A prospective study," *Cancer Imaging*, vol. 23, no. 1, p. 61, 2023.

[11] A. E. Campbell-Washburn, M. A. Tavallaei, M. Pop, *et al.*, "Real-time mri guidance of cardiac interventions," *Journal of Magnetic Resonance Imaging*, vol. 46, no. 4, pp. 935–950, 2017.

[12] X. Li, J. Li, N. Zheng, H. Hu, X. Xie, and G. Huang, "Ultrasound fusion–guided core needle biopsy for deep head and neck space lesions: Technical feasibility, histopathologic yield, and safety," *American Journal of Neuroradiology*, vol. 44, no. 2, pp. 180–185, 2023.

[13] I. Hirata, A. Mazzotta, P. Makvandi, *et al.*, "Sensing technologies for extravasation detection: A review," *ACS sensors*, vol. 8, no. 3, pp. 1017–1032, 2023.

[14] M. Wysocki, M. F. Azampour, C. Eilers, B. Busam, M. Salehi, and N. Navab, "Ultra-nerf: Neural radiance fields for ultrasound imaging," in *Medical Imaging with Deep Learning*, PMLR, 2024, pp. 382–401.

[15] V. Mishra, H. Bouayad, A. Schned, A. Hartov, J. Heaney, and R. J. Halter, "A real-time electrical impedance sensing biopsy needle," *IEEE transactions on biomedical engineering*, vol. 59, no. 12, pp. 3327–3336, 2012.

[16] K. Watanabe, J. Tokumine, A. K. Lefor, *et al.*, "Photoacoustic needle improves needle tip visibility during deep peripheral nerve block," *Scientific Reports*, vol. 11, no. 1, p. 8432, 2021.

[17] C. Shi, V. Andino-Pavlovsky, S. A. Lee, *et al.*, "Application of a sub–0.1-mm3 implantable mote for in vivo real-time wireless temperature sensing," *Science Advances*, vol. 7, no. 19, eabf6312, 2021.

[18] A. L. Robert, G. Chagnon, A. Bonvilain, P. Cinquin, and A. Moreau-Gaudry, "Toward a real-time tracking of a medical deformable needle from strain measurements," in *2013 35th Annual International Conference of the IEEE Engineering in Medicine and Biology Society (EMBC)*, IEEE, 2013, pp. 3495–3498.

[19] B. Zhang, F. Chen, M. Yang, *et al.*, "Real-time curvature detection of a flexible needle with a bevel tip," *Sensors*, vol. 18, no. 7, p. 2057, 2018.

[20] M. Vucevic, B. Tehan, F. Gamlin, J. Berridge, and M. Boylan, "The smart needle: A new doppler ultrasound-guided vascular access needle," *Anaesthesia*, vol. 49, no. 10, pp. 889–891, 1994.

[21] E. Evangelisti, E. Schena, C. Massaroni, *et al.*, "Experimental analysis of the influencing factors on the response of a tool for epidural space detection," in *2018 IEEE International Symposium on Medical Measurements and Applications (MeMeA)*, IEEE, 2018, pp. 1–5.

[22] Z. Cheng, S. L. B. Sørensen, M. W. Olsen, R. L. Eriksen, and T. R. Savarimuthu, "Needle tip tracking based on optical imaging and ai," *IEEE Sensors Journal*, 2024.

[23] D. Dall'Alba, B. Maris, and P. Fiorini, "A compact navigation system for free hand needle placement in percutaneos procedures," in *2012 IEEE/RSJ International Conference on Intelligent Robots and Systems*, IEEE, 2012, pp. 2013–2018.

[24] R. Nachabé, B. H. Hendriks, R. Schierling, *et al.*, "Real-time in vivo characterization of primary liver tumors with diffuse optical spectroscopy during percutaneous needle interventions: Feasibility study in woodchucks," *Investigative radiology*, vol. 50, no. 7, pp. 443–448, 2015.

[25] V. Virdyawan, M. Oldfield, and F. R. y Baena, "Laser doppler sensing for blood vessel detection with a biologically inspired steerable needle," *Bioinspiration & biomimetics*, vol. 13, no. 2, p. 026 009, 2018.

[26] R. Mieling, C. Stapper, S. Gerlach, *et al.*, "Proximity-based haptic feedback for collaborative robotic needle insertion," in *International Conference on Human Haptic Sensing and Touch Enabled Computer Applications*, Springer, 2022, pp. 301–309.

[27] D. A. Lezcano, M. J. Kim, I. I. Iordachita, and J. S. Kim, "Toward fbg-sensorized needle shape prediction in tissue insertions," in *2022 IEEE/RSJ International Conference on Intelligent Robots and Systems (IROS)*, IEEE, 2022, pp. 3505–3511.

[28] Northern Digital Inc., *Optical navigation technology / optical tracking - ndi*, `https://www.ndigital.com/optical-navigation-technology/`, 2024.

[29] V. Virdyawan and F. R. Y. Baena, "Vessel pose estimation for obstacle avoidance in needle steering surgery using multiple forward looking sensors," in *2018 IEEE/RSJ International Conference on Intelligent Robots and Systems (IROS)*, IEEE, 2018, pp. 3845–3852.

[30] L. Schoevaerdts, G. Borghesan, M. Ourak, D. Reynaerts, and E. Vander Poorten, "Electrical bio-impedance proximity sensing for vitreo-retinal micro-surgery," *IEEE Robotics and Automation Letters*, vol. 4, no. 4, pp. 4086–4093, 2019.

[31] L. Schoevaerdts, L. Esteveny, A. Gijbels, J. Smits, D. Reynaerts, and E. Vander Poorten, "Design and evaluation of a new bioelectrical impedance sensor for micro-surgery: Application to retinal vein cannulation," *International journal of computer assisted radiology and surgery*, vol. 14, no. 2, pp. 311–320, 2019.

[32] B. Carotenuto, A. Micco, A. Ricciardi, *et al.*, "Optical guidance systems for epidural space identification," *IEEE Journal of Selected Topics in Quantum Electronics*, vol. 23, no. 2, pp. 371–379, 2016.

[33] S. Ambastha, S. Umesh, S. Dabir, and S. Asokan, "Comparison of force required for lumbar puncture with different gauges of spinal needle using fiber bragg grating force device," *IEEE Sensors Journal*, vol. 18, no. 19, pp. 8028–8033, 2018.

[34] *Ascension trakSTAR - Tracklab — freedspace.com.au*, `https://freedspace.com.au/tracklab/products/brands/ndi/ascension-trakstar/`, 2025.

[35] Z. Zhao and Z. T. H. Tse, "An electromagnetic tracking needle clip: An enabling design for low-cost image-guided therapy," *Minimally Invasive Therapy & Allied Technologies*, vol. 28, no. 3, pp. 165–171, 2019.

[36] A. N. Johnson, J. S. Peiffer, N. Halmann, L. Delaney, C. A. Owen, and J. Hersh, "Ultrasound-guided needle technique accuracy: Prospective comparison of passive magnetic tracking versus unassisted echogenic needle localization," *Regional Anesthesia & Pain Medicine*, vol. 42, no. 2, pp. 223–232, 2017.

[37] M. Srivastava, K. O'Donoghue, A. Sidun, *et al.*, "3d position tracking using on-chip magnetic sensing in image-guided navigation bronchoscopy," *IEEE Transactions on Biomedical Circuits and Systems*, 2024.

[38] L. Grau-Mercier, A. Chetioui, L. Muller, *et al.*, "Magnetic needle-tracking device for ultrasound guidance of radial artery puncture: A randomized study on a simulation model," *Journal of Clinical Ultrasound*, vol. 49, no. 3, pp. 212–217, 2021.

[39] H. Kalvøy and A. R. Sauter, "Detection of intraneural needle-placement with multiple frequency bioimpedance monitoring: A novel method," *Journal of clinical monitoring and computing*, vol. 30, pp. 185–192, 2016.

[40] J. Yun, G. Kang, Y. Park, H. W. Kim, J.-J. Cha, and J.-H. Lee, "Electrochemical impedance spectroscopy with interdigitated electrodes at the end of hypodermic needle for depth profiling of biotissues," *Sensors and Actuators B: Chemical*, vol. 237, pp. 984–991, 2016.

[41] J. Yun, H. W. Kim, and J.-H. Lee, "Improvement of depth profiling into biotissues using micro electrical impedance spectroscopy on a needle with selective passivation," *Sensors*, vol. 16, no. 12, p. 2207, 2016.

[42] Z. Cheng, B. L. Davies, D. G. Caldwell, and L. S. Mattos, "A hand-held robot for precise and safe pivc," *IEEE Robotics and Automation Letters*, vol. 4, no. 2, pp. 655–661, 2019.

[43] *Injeq IQ-Tip® spinal needle | Injeq IQ-Tip® Lumbar puncture technique using CSF detection — injeq.com*, `https://injeq.com/`, 2025.

[44] J. Park, W.-M. Choi, K. Kim, W.-I. Jeong, J.-B. Seo, and I. Park, "Biopsy needle integrated with electrical impedance sensing microelectrode array towards real-time needle guidance and tissue discrimination," *Scientific reports*, vol. 8, no. 1, p. 264, 2018.

[45] J. Park, J. R. Sempionatto, J. Kim, *et al.*, "Microscale biosensor array based on flexible polymeric platform toward lab-on-a-needle: Real-time multiparameter biomedical assays on curved needle surfaces," *ACS sensors*, vol. 5, no. 5, pp. 1363–1373, 2020.

[46] R. Lin, Y. Jin, R. R. Li, *et al.*, "Needle-integrated ultrathin bioimpedance microsensor array for early detection of extravasation," *Biosensors and Bioelectronics*, vol. 216, p. 114 651, 2022.

[47] D. J. Hernandez, V. A. Sinkov, W. W. Roberts, *et al.*, "Measurement of bio-impedance with a smart needle to confirm percutaneous kidney access," *The Journal of urology*, vol. 166, no. 4, pp. 1520–1523, 2001.

[48] D. Trebbels, F. Fellhauer, M. Jugl, G. Haimerl, M. Min, and R. Zengerle, "Online tissue discrimination for transcutaneous needle guidance applications using broadband impedance spectroscopy," *IEEE transactions on biomedical engineering*, vol. 59, no. 2, pp. 494–503, 2011.

[49] S. Halonen, J. Kari, P. Ahonen, T. Elomaa, P. Annus, and K. Kronstrom, "Biopsy needle including bioimpedance probe with optimized sensitivity distribution," *Int. J. Bioelectromagn*, vol. 17, no. 1, pp. 26–30, 2015.

[50] Y. Wu, F. F. Hanzaee, D. Jiang, R. H. Bayford, and A. Demosthenous, "Electrical impedance tomography for biomedical applications: Circuits and systems review," *IEEE Open Journal of Circuits and Systems*, vol. 2, pp. 380–397, 2021.

[51] J. Park, Y. Jeong, J. Kim, J. Gu, J. Wang, and I. Park, "Biopsy needle integrated with multimodal physical/chemical sensor array," *Biosensors and Bioelectronics*, vol. 148, p. 111 822, 2020.

[52] N. Chen, L. Tian, A. C. Patil, *et al.*, "Neural interfaces engineered via micro-and nanostructured coatings," *Nano Today*, vol. 14, pp. 59–83, 2017.

[53] C. C. Maglioli, D. G. Caldwell, and L. S. Mattos, "A bioimpedance sensing system for in-vivo cancer tissue identification: Design and preliminary evaluation," in *2017 39th Annual International Conference of the IEEE Engineering in Medicine and Biology Society (EMBC)*, IEEE, 2017, pp. 4235–4238.

[54] Z. Cheng, B. L. Davies, D. G. Caldwell, G. Barresi, Q. Xu, and L. S. Mattos, "A hand-held robotic device for peripheral intravenous catheterization," *Proceedings of the Institution of Mechanical Engineers, Part H: Journal of Engineering in Medicine*, vol. 231, no. 12, pp. 1165–1177, 2017.

[55] Z. Cheng, B. L. Davies, D. G. Caldwell, and L. S. Mattos, "A new venous entry detection method based on electrical bio-impedance sensing," *Annals of biomedical engineering*, vol. 46, pp. 1558–1567, 2018.

[56] Z. Cheng, B. L. Davies, D. G. Caldwell, and L. S. Mattos, "Sdop: A smart handheld device for over puncture prevention during pediatric peripheral intravenous catheterization," in *2018 International Symposium on Medical Robotics (ISMR)*, IEEE, 2018, pp. 1–6.

[57] Z. Cheng, A. L. C. Carobbio, L. Soggiu, *et al.*, "Smartprobe: A bioimpedance sensing system for head and neck cancer tissue detection," *Physiological measurement*, vol. 41, no. 5, p. 054 003, 2020.

[58] L. Helen, B. D. O'Donnell, W. Messina, C. O'Mahony, O. M. Ahmed, and E. J. Moore, "Impedance sensor to detect substance change at the needle tip," *Electroanalysis*, vol. 29, no. 11, pp. 2533–2540, 2017.

[59] S. Halonen, J. Kari, P. Ahonen, K. Kronström, and J. Hyttinen, "Real-time bioimpedance-based biopsy needle can identify tissue type with high spatial accuracy," *Annals of biomedical engineering*, vol. 47, no. 3, pp. 836–851, 2019.

[60] A. C. Lazanas and M. I. Prodromidis, "Electrochemical impedance spectroscopy— a tutorial," *ACS measurement science au*, vol. 3, no. 3, pp. 162–193, 2023.

[61] P. Kassanos, "Bioimpedance sensors: A tutorial," *IEEE Sensors Journal*, vol. 21, no. 20, pp. 22 190–22 219, 2021.

[62] O. G. Martinsen, S. Grimnes, H. P. Schwan, *et al.*, "Interface phenomena and dielectric properties of biological tissue," *Encyclopedia of surface and colloid science*, vol. 20, pp. 2643–2653, 2002.

[63] D. Naranjo-Hernández, J. Reina-Tosina, and M. Min, "Fundamentals, recent advances, and future challenges in bioimpedance devices for healthcare applications," *Journal of Sensors*, vol. 2019, no. 1, p. 9 210 258, 2019.

[64] N. Gao, W. Zhou, X. Jiang, G. Hong, T.-M. Fu, and C. M. Lieber, "General strategy for biodetection in high ionic strength solutions using transistor-based nanoelectronic sensors," *Nano letters*, vol. 15, no. 3, pp. 2143–2148, 2015.

[65] W. Franks, I. Schenker, P. Schmutz, and A. Hierlemann, "Impedance characterization and modeling of electrodes for biomedical applications," *IEEE Transactions on Biomedical Engineering*, vol. 52, no. 7, pp. 1295–1302, 2005.

[66] P. Kassanos, A. Demosthenous, and R. H. Bayford, "Optimization of bipolar and tetrapolar impedance biosensors," in *Proceedings of 2010 IEEE International Symposium on Circuits and Systems*, IEEE, 2010, pp. 1512–1515.

[67] S. M. Radke and E. C. Alocilja, "Design and fabrication of a microimpedance biosensor for bacterial detection," *IEEE sensors journal*, vol. 4, no. 4, pp. 434–440, 2004.

[68] P. Kassanos and I. F. Triantis, "A cmos multi-sine signal generator for multi-frequency bioimpedance measurements," in *2014 IEEE International Symposium on Circuits and Systems (ISCAS)*, IEEE, 2014, pp. 249–252.

[69] *Analog.com*, `https://www.analog.com/media/en/technical-documentation/data-sheets/ad5940-5941.pdf`.

[70] P. O. Gaggero, A. Adler, J. Brunner, and P. Seitz, "Electrical impedance tomography system based on active electrodes," *Physiological measurement*, vol. 33, no. 5, p. 831, 2012.

[71] P. Kassanos and G.-Z. Yang, "A cmos programmable phase shifter for compensating synchronous detection bioimpedance systems," in *2017 24th IEEE International Conference on Electronics, Circuits and Systems (ICECS)*, IEEE, 2017, pp. 218–221.

[72] Y. Wu, D. Jiang, A. Bardill, S. De Gelidi, R. Bayford, and A. Demosthenous, "A high frame rate wearable eit system using active electrode asics for lung respiration and heart rate monitoring," *IEEE Transactions on Circuits and Systems I: Regular Papers*, vol. 65, no. 11, pp. 3810–3820, 2018.

[73] M. Zamani, Y. Rezaeiyan, O. Shoaei, and W. A. Serdijn, "A 1.55 μw bio-impedance measurement system for implantable cardiac pacemakers in 0.18 μm cmos," *IEEE Transactions on Biomedical Circuits and Systems*, vol. 12, no. 1, pp. 211–221, 2018.

[74] N. Neshatvar, P. Langlois, R. Bayford, and A. Demosthenous, "Analog integrated current drivers for bioimpedance applications: A review," *Sensors*, vol. 19, no. 4, p. 756, 2019.

[75] A. Rao, E. K. Murphy, R. J. Halter, and K. M. Odame, "A 1 mhz miniaturized electrical impedance tomography system for prostate imaging," *IEEE transactions on biomedical circuits and systems*, vol. 14, no. 4, pp. 787–799, 2020.

[76] M. Konijnenburg, S. Stanzione, L. Yan, *et al.*, "A multi (bio) sensor acquisition system with integrated processor, power management, 8 x 8 led drivers, and simultaneously synchronized ecg, bio-z, gsr, and two ppg readouts," *IEEE Journal of Solid-State Circuits*, vol. 51, no. 11, pp. 2584–2595, 2016.

[77] P. Kassanos, L. Constantinou, I. F. Triantis, and A. Demosthenous, "An integrated analog readout for multi-frequency bioimpedance measurements," *IEEE Sensors Journal*, vol. 14, no. 8, pp. 2792–2800, 2014.

[78] Y. Wu, D. Jiang, M. Habibollahi, N. Almarri, and A. Demosthenous, "Time stamp–a novel time-to-digital demodulation method for bioimpedance implant applications," *IEEE Transactions on Biomedical Circuits and Systems*, vol. 14, no. 5, pp. 997–1007, 2020.

[79] H. Ha, C. Van Hoof, and N. Van Helleputte, "Measurement and analysis of input-signal dependent flicker noise modulation in chopper stabilized instrumentation amplifier," *IEEE Solid-State Circuits Letters*, vol. 1, no. 4, pp. 90–93, 2018.

[80] H. Zhong, Z. Teng, J. Sang, Q. Tang, B. Liu, and S. B. Rutkove, "A general and accurate impedance demodulation method based on improved dft for electrical impedance spectrometer," *IEEE Transactions on Industrial Informatics*, 2024.

[81] M. L. Balter, A. I. Chen, T. J. Maguire, and M. L. Yarmush, "Adaptive kinematic control of a robotic venipuncture device based on stereo vision, ultrasound, and force guidance," *IEEE Transactions on Industrial Electronics*, vol. 64, no. 2, pp. 1626–1635, 2016.

[82] M. Koskinopoulou, A. Acemoglu, V. Penza, and L. S. Mattos, "Dual robot collaborative system for autonomous venous access based on ultrasound and bioimpedance sensing technology," in *2023 IEEE International Conference on Robotics and Automation (ICRA)*, IEEE, 2023, pp. 4648–4653.

[83] M. Souto-Romero, J. Pelegrín-Borondo, M. Arias-Oliva, and A. A. Almahameed, "Consumer acceptance of robotic surgeons in health services," *Humanities and Social Sciences Communications*, vol. 11, no. 1, pp. 1–11, 2024.

[84] B. Szabó, B. Őrsi, and C. Csukonyi, "Robots for surgeons? surgeons for robots? exploring the acceptance of robotic surgery in the light of attitudes and trust in robots," *BMC psychology*, vol. 12, no. 1, p. 45, 2024.

[85] J. Haltaufderheide, S. Pfisterer-Heise, D. Pieper, and R. Ranisch, "The ethical landscape of robot-assisted surgery: A systematic review," *Journal of Robotic Surgery*, vol. 19, no. 1, p. 102, 2025.

[86] J. M. Leipheimer, M. L. Balter, A. I. Chen, *et al.*, "First-in-human evaluation of a hand-held automated venipuncture device for rapid venous blood draws," *Technology*, vol. 7, no. 03n04, pp. 98–107, 2019.

[87] R. Mieling, M. Neidhardt, S. Latus, *et al.*, "Collaborative robotic biopsy with trajectory guidance and needle tip force feedback," in *2023 IEEE International Conference on Robotics and Automation (ICRA)*, IEEE, 2023, pp. 6893–6900.

[88] C. Quesada, I. Alfaro, D. González, F. Chinesta, and E. Cueto, "Haptic simulation of tissue tearing during surgery," *International journal for numerical methods in biomedical engineering*, vol. 34, no. 3, e2926, 2018.

[89] M. Ríos-Hernández, J. M. Jacinto-Villegas, N. Zemiti, A. H. Vilchis-González, M. A. Padilla-Castañeda, and B. Debien, "Development of a lumbar puncture virtual simulator for medical students training: A preliminary evaluation," *The International Journal of Medical Robotics and Computer Assisted Surgery*, vol. 19, no. 6, e2572, 2023.

[90] G. Ravali and M. Manivannan, "Haptic feedback in needle insertion modeling and simulation," *IEEE reviews in biomedical engineering*, vol. 10, pp. 63–77, 2017.

[91] *Sim&Care - Daily medical gesture simulation — insimo.com*, `https://www.insimo.com/sim-care/`, 2025.

[92] *Dielectric Properties of Body Tissues: HTML clients — niremf.ifac.cnr.it*, `http://niremf.ifac.cnr.it/tissprop/htmlclie/htmlclie.php`, 2025.

[93] Y. Luo, D. Huang, Z.-Y. Huang, T. K. Hsiai, and Y.-C. Tai, "An ex vivo study of outward electrical impedance tomography (oeit) for intravascular imaging," *IEEE Transactions on Biomedical Engineering*, vol. 69, no. 2, pp. 734–745, 2021.

[94] M. Shen, J. Sun, P. Suo, *et al.*, "Image reconstruction in open-eit by combining inversion mapping and sparse contour representation," *IEEE Transactions on Instrumentation and Measurement*, vol. 73, pp. 1–9, 2024.

[95] M. Zamani, M. Kallio, R. Bayford, and A. Demosthenous, "Generation of anatomically inspired human airway tree using electrical impedance tomography: A method to estimate regional lung filling characteristics," *IEEE Transactions on Medical Imaging*, vol. 41, no. 5, pp. 1125–1137, 2021.

[96] M. Luo, X. Yang, H. Wang, L. Du, and D. Ni, "Deep motion network for freehand 3d ultrasound reconstruction," in *International Conference on Medical Image Computing and Computer-Assisted Intervention*, Springer, 2022, pp. 290–299.

[97] H. Chen, L. Kumaralingam, S. Zhang, *et al.*, "Neural implicit surface reconstruction of freehand 3d ultrasound volume with geometric constraints," *Medical Image Analysis*, vol. 98, p. 103 305, 2024.

[98] *3D Slicer image computing platform — slicer.org*, `https://www.slicer.org/`, 2025.

[99] M. Yu, W. Ding, G. Shao, *et al.*, "Application of a nerve stereoscopic reconstruction technique based on ultrasonic images in the diagnosis of neuralgic amyotrophy," *Frontiers in Physiology*, vol. 14, p. 1 201 275, 2023.

[100] L. Pušnik, L. Lechner, I. Serša, *et al.*, "3d fascicular reconstruction of median and ulnar nerve: Initial experience and comparison between high-resolution ultrasound and mr microscopy," *European Radiology Experimental*, vol. 8, no. 1, p. 100, 2024.

[101] J. Van Boxtel, V. Vousten, J. Pluim, and N. M. Rad, "Hybrid deep neural network for brachial plexus nerve segmentation in ultrasound images," in *2021 29th European Signal Processing Conference (EUSIPCO)*, IEEE, 2021, pp. 1246–1250.

[102] M. Luo, X. Yang, Z. Yan, *et al.*, "Multi-imu with online self-consistency for freehand 3d ultrasound reconstruction," in *International conference on medical image computing and computer-assisted intervention*, Springer, 2023, pp. 342–351.

[103] S. Fadnavis, A. Chowdhury, J. Batson, P. Drineas, and E. Garyfallidis, "Patch2self2: Self-supervised denoising on coresets via matrix sketching," in *Proceedings of the IEEE/CVF Conference on Computer Vision and Pattern Recognition*, 2024, pp. 27 641–27 651.

[104] M. Zamani and A. Demosthenous, "Deepnav: Joint view learning for direct optimal path perception in cochlear surgical platform navigation," *IEEE Access*, vol. 11, pp. 120 593–120 602, 2023.

[105] T. Abbasi-Hashemi, F. Janabi-Sharifi, A. N. Cheema, and K. Zareinia, "A haptic guidance system for simulated catheter navigation with different kinaesthetic feedback profiles," *The International Journal of Medical Robotics and Computer Assisted Surgery*, vol. 20, no. 3, e2638, 2024.